Commun. Comput. Phys.
doi: 10.4208/cicp.111013.120914a

Vol. **17**, No. 2, pp. 337-370
February 2015

Simulation of Earthquake Rupture Dynamics in Complex Geometries Using Coupled Finite Difference and Finite Volume Methods

Ossian O'Reilly[1,2,*], Jan Nordström[2], Jeremy E. Kozdon[3] and Eric M. Dunham[1,4]

[1] *Department of Geophysics, Stanford University, CA 94305-2215, USA.*
[2] *Department of Mathematics, Division of Computational Mathematics, Linköping University, SE-581 83 Linköping, Sweden.*
[3] *Department of Applied Mathematics, Naval Postgraduate School, Monterey, CA 93943-5216, USA.*
[4] *Institute for Computational and Mathematical Engineering, Stanford University, CA 94305-4042, USA.*

Received 11 October 2013; Accepted (in revised version) 12 September 2014

Abstract. We couple a node-centered finite volume method to a high order finite difference method to simulate dynamic earthquake ruptures along nonplanar faults in two dimensions. The finite volume method is implemented on an unstructured mesh, providing the ability to handle complex geometries. The geometric complexities are limited to a small portion of the overall domain and elsewhere the high order finite difference method is used, enhancing efficiency. Both the finite volume and finite difference methods are in summation-by-parts form. Interface conditions coupling the numerical solution across physical interfaces like faults, and computational ones between structured and unstructured meshes, are enforced weakly using the simultaneous-approximation-term technique. The fault interface condition, or friction law, provides a nonlinear relation between fields on the two sides of the fault, and allows for the particle velocity field to be discontinuous across it. Stability is proved by deriving energy estimates; stability, accuracy, and efficiency of the hybrid method are confirmed with several computational experiments. The capabilities of the method are demonstrated by simulating an earthquake rupture propagating along the margins of a volcanic plug.

AMS subject classifications: 35L05, 35L65, 35Q35, 65M06, 65M08, 65M12, 65Z05

Key words: Elastic waves, earthquake, high order finite difference finite volume, summation-by-parts, simultaneous approximation term, nonlinear boundary conditions.

*Corresponding author. *Email addresses:* ooreilly@stanford.edu (O. O'Reilly), jan.nordstrom@liu.se (J. Nordström), jekozdon@nps.edu (J. E. Kozdon), edunham@stanford.edu (E. M. Dunham)

 ©2015 Global-Science Press

https://doi.org/10.4208/cicp.111013.120914a Published online by Cambridge University Press

1 Introduction

Computational modeling of earthquake rupture dynamics presents many challenges. Like similar radiation problems in electrodynamics and other fields, there is particular interest in waves in the far field, as most observations are made at distances many wavelengths away from a compact source region. This argues for the use of high order methods with minimal dispersion errors. However, in dynamic rupture models, the source process itself is not known a priori, but is determined as part of the solution. To be more specific, seismic (i.e., elastic) waves are generated by slip across fault surfaces (i.e., the discontinuity in the tangential component of the displacement field across an internal interface). Slip on one part of the fault excites waves that transmit stresses to adjacent parts of the fault, possibly triggering slip there and leading to the progressive propagation of a rupture. The condition for fault slip is typically expressed as a nonlinear friction law coupling fault slip velocity and tractions acting on the sides of the fault. Further challenges arise from the geometrical complexity of natural fault geometries, often involving multiple nonplanar surfaces with kinks and branches. Numerical methods based on unstructured meshes are well suited to handle this level of complexity in the near field source region. The challenge, then, is to combine the advantages of numerical methods based on unstructured meshes (for the near field or source region) with high order numerical methods based on structured grids (for the far field region), in an accurate and stable manner.

A variety of other numerical approaches have been taken to study earthquake rupture dynamics, each with benefits and shortcomings. Some of the more recent numerical approaches we will describe have been, or are actively being, verified and evaluated using a series of benchmark exercises as part of the Southern California Earthquake Center/U.S. Geological Survey (SCEC/USGS) Dynamic Earthquake Rupture Code Verification Project [28]. Traditionally, finite difference methods have been widely used, but mostly for planar faults (e.g., [3, 16, 42, 44, 69]). In more recent years, nonplanar fault geometries have also been incorporated in finite difference methods using coordinate transform techniques (e.g., [14, 15, 36]). In the coordinate transform method developed in [36], the physical domain is decomposed into multiple curvilinear blocks that conform to nonplanar surfaces. Each block is mapped onto a rectangle or square in the computational domain, and the transformed equations are solved in the computational domain with finite differences. Severe grid skewness, for instance due to intersecting faults with small angles, can cause the transform to be poorly conditioned. Thus, it can be difficult to develop well-conditioned multi-block decompositions of geometries that arise in realistic fault systems. Boundary element methods have also been developed (e.g., [4, 22, 32, 64, 70]). Solutions given by these methods are limited to faults in a uniform medium and some can develop numerical instabilities. These methods can handle nonplanar faults, except for the spectral boundary integral equation method [22]. However, the spectral boundary integral equation method is quite efficient and accurate for planar fault problems, and has been widely used to investigate realistic fault weakening

https://doi.org/10.4208/cicp.111013.120914a Published online by Cambridge University Press

processes.

Many of the challenges involved with using finite difference methods and boundary integral equation methods in complex geometries can be overcome using unstructured mesh methods. The use of unstructured meshes offers flexibility to discretize complex fault geometries, heterogeneous material properties, and topography at the expense of mesh preprocessing, increased computational work, and implementation complexity (as compared to structured grid methods). Several unstructured mesh methods have been developed for earthquake rupture dynamics in complex geometries, using finite element methods (e.g., [1, 7, 18, 19, 40, 66, 67]), finite volume methods (e.g., [8, 9]), spectral element methods (e.g., [20,30,33]) and discontinuous Galerkin methods (e.g., [17,34,55,65]). While continuous Galerkin finite element methods have been quite effective for modeling fault rupture, in practice these methods have been limited to 2^{nd}-order accuracy (a computational choice for efficient mass matrix inversion). Since 2^{nd}-order accurate methods are not ideal in resolving far field waves, high order finite element methods have also been considered, in particular (quad and hex based) spectral element and discontinuous Galerkin methods. Spectral elements have the advantage of having a diagonal mass matrix, but those used for rupture dynamics currently require a global quadrilateral or hexahedral mesh which can be difficult to generate in practice for realistic fault geometries [68]. The discontinuous Galerkin method on the other hand has an element local (globally block diagonal) mass matrix [29]. To achieve this, the solution is allowed to be discontinuous across the element interface, which requires a doubling of the number of degrees of freedom along the element edges. More importantly though, there is a significant time step restriction for high order versions.

In this work, we develop a hybrid finite volume-finite difference method based on summation-by-parts (SBP) difference operators [12, 38, 39, 54, 59, 63]. This finite volume method uses unstructured meshes and treats complex geometry with the same flexibility as finite element methods. Other hybrid methods, combining finite elements and finite differences, have been developed for earthquake rupture dynamics (e.g., [6, 41, 44]), but require the use of overlapping grids and have no associated proofs of stability. In contrast, by utilizing properties of SBP operators here we develop a provably stable hybrid method based on coupling at grid interfaces (i.e., the grids are non-overlapping). We do this by imposing interface (and boundary) conditions weakly using the simultaneous approximation term (SAT) method [10]. When the penalty terms are properly chosen, the numerical method is provably stable; the penalty terms in SAT and closely related the fluxes in discontinuous Galerkin methods [21].

The SBP-SAT formulation, which was originally developed for fluid [50, 53, 60, 62] and wave propagation problems [2, 43, 51], has been used to develop a stable and accurate finite difference method for earthquake rupture dynamics in complex geometries using multiblock grids [35, 36]. That said, well-conditioned multiblock decompositions of realistic fault geometries can be difficult to develop. The hybrid approach we propose here overcomes many of these difficulties. The node-centered finite-volume method was shown to be an SBP scheme in [48] and has been coupled to high order finite difference

https://doi.org/10.4208/cicp.111013.120914a Published online by Cambridge University Press

methods for both advection [49] and advection-diffusion [23,52] problems. Here we extend the coupling to the scalar wave equation (written in first order form for velocities and stresses). Additionally, we show how nonlinear friction laws can be handled in the unstructured finite volume method. Extensions of the developed method would permit modeling of rupture dynamics and wave propagation in 2-D plane strain and even 3-D geometries, though these extensions are beyond the scope of this initial study.

The organization of this paper is as follows: in Section 2, we present the continuous formulation of the 2-D linear elastic antiplane shear problem, including interface conditions and boundary conditions as well as the energy balance. The SBP operators are introduced in Section 3, and the semi-discrete problem is formulated. Finally, in Section 4, we conduct numerical experiments to verify the stability and accuracy of our numerical implementation.

2 Continuous problem

While the method we develop can be applied to general problems involving geometrically complex fault networks, we focus here on the specific case of earthquake ruptures along the edges of a crystalline plug within a volcanic conduit. Swarms of repeating drumbeat earthquakes (so-called because of their regular recurrence interval of a few minutes) occurred during the 2004-2008 effusive eruption of Mount Saint Helens, Washington. These events are possibly explained by slip along the walls of a plug that was extruded from the vent [31,45]. Fig. 1 illustrates a volcanic conduit with a solidified plug. The plug margin serves as a fault, hosting small earthquakes triggered by the pressurization of magma beneath it. Dynamics of the plug are governed by the forces acting on it, as well as the elastic response of the plug and surrounding material. More details are given in Section 5.

We begin by considering a horizontal cross-section Ω of a plug within a volcanic conduit (Figs. 1 and 2). The plug is located in the center of the domain Ω. For simplicity, both the plug and the surrounding volcanic conduit are modeled as the same homogeneous, elastic materials. The contour γ is the interface between the plug and the surrounding material, referred to as the plug margin. We use the superscript (2) to denote the plug, and superscript (1) to denote the surrounding material. The rectangular computational domain, Ω, has outer boundary $\partial\Omega$.

We neglect variations of fields in the vertical direction, thereby reducing the problem to two-dimensional antiplane shear deformation. The dimensionless governing equations within the plug and surrounding material are

$$\frac{\partial v_z}{\partial t}=\frac{\partial \sigma_{xz}}{\partial x}+\frac{\partial \sigma_{yz}}{\partial y}, \tag{2.1}$$

$$\frac{\partial \sigma_{xz}}{\partial t}=\frac{\partial v_z}{\partial x}, \quad \frac{\partial \sigma_{yz}}{\partial t}=\frac{\partial v_z}{\partial y}, \tag{2.2}$$

https://doi.org/10.4208/cicp.111013.120914a Published online by Cambridge University Press

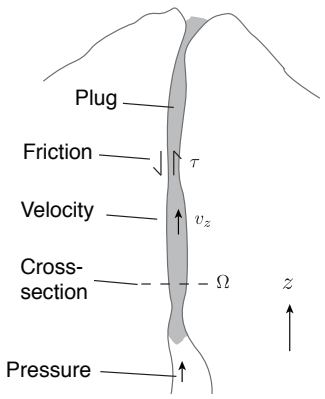


Figure 1: Solidified plug within a volcanic conduit hosting earthquakes along its margins. Upward extrusion of the plug is driven by pressure from magma beneath it and resisted by its weight and friction along the plug walls.

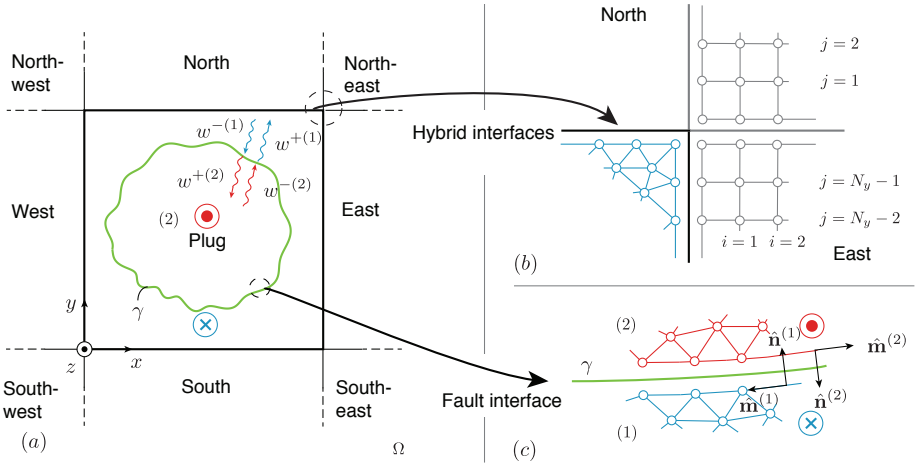


Figure 2: (a) Cross-section of the plug (1) and surrounding rocks (2); both materials have linear elastic response, with friction acting along their common interface γ. (b) A hybrid mesh. Since the plug makes up a small fraction of the entire computational domain, only the plug and vicinity are resolved with unstructured meshes. The rest of the computational domain is resolved with structured grids. The unstructured meshes are coupled to structured grids along the Cartesian boundaries shown in bold, solid black lines. (c) Across the fault γ some of the fields can be discontinuous. All interfaces (hybrid interfaces and fault interfaces) have collocated nodes (illustrated in the upper-right panel).

Eqs. (2.1) and (2.2) have been nondimensionalized in terms of a characteristic length h^* and corresponding time scale h^*/c, where c is the shear-wave speed $c=\sqrt{G/\rho}$, with G and ρ being the shear modulus and the density, respectively; both G and ρ are taken to be constant in this work. The characteristic stress and velocity scales are linked by the shear-wave impedance ρc. In Eq. (2.1), $v_z(x,y,t)$ is the $\hat{\mathbf{z}}$-component (out of the page or vertical) of the particle velocity, and the shear stress components $\sigma_{xz}(x,y,t)$ and $\sigma_{yz}(x,y,t)$ are those exerting tractions in the $\hat{\mathbf{z}}$-direction on planes with unit normals $\hat{\mathbf{x}}$ and $\hat{\mathbf{y}}$, respectively.

https://doi.org/10.4208/cicp.111013.120914a Published online by Cambridge University Press

With dimensional fields, Eq. (2.1), with the left-hand side multiplied by density ρ, is conservation of momentum, and Eq. (2.2), with the right-hand side multiplied by shear modulus G, is the time derivative of Hooke's law.

We use the energy method to show well-posedness of the continuous problem and stability of the numerical discretization, and for this analysis it is convenient to write governing equations (2.1) and (2.2) in matrix form:

$$\frac{\partial \mathbf{q}}{\partial t}=\mathbf{A}_x\frac{\partial \mathbf{q}}{\partial x}+\mathbf{A}_y\frac{\partial \mathbf{q}}{\partial y},\qquad \mathbf{q}=\left[v_z,\,\sigma_{xz},\,\sigma_{yz}\right]^T,$$
$$\mathbf{A}_x=\begin{bmatrix}0&1&0\\1&0&0\\0&0&0\end{bmatrix},\qquad \mathbf{A}_y=\begin{bmatrix}0&0&1\\0&0&0\\1&0&0\end{bmatrix}. \tag{2.3}$$

2.1 Boundary and interface conditions

For hyperbolic equations it is well known that the number of boundary conditions required is equal to the number of characteristic variables entering the domain [37]. Similarly, for domains that are partitioned into multiple subdomains, the number of interface conditions needed is equal to the number of characteristic variables entering each subdomain from the interface. That is, we can specify conditions on the characteristic variables resulting from the diagonalization of $\mathbf{A}_i n_i$, where summation over x and y is implied by repeating indices ($\mathbf{A}_i n_i=\mathbf{A}_x n_x+\mathbf{A}_y n_y$) with $\hat{\mathbf{n}}=\left[n_x,\,n_y\right]^T$ being the outward unit normal with respect to the subdomain boundary of interest. The outward unit normal $\hat{\mathbf{n}}$ is orthogonal to the unit tangent vector $\hat{\mathbf{m}}=\left[n_y,\,-n_x\right]^T$, satisfying $\hat{\mathbf{z}}=\hat{\mathbf{n}}\times\hat{\mathbf{m}}$. The diagonalization results in the characteristic variables

$$w^{\pm}=\sigma_{iz}n_i\mp v_z\quad\text{and}\quad w^0=\sigma_{iz}m_i. \tag{2.4}$$

Characteristic variables $w^{\pm}$ are those propagating in the $\pm\hat{\mathbf{n}}$-directions with unit speed (and speed c in dimension form) and w^0 is a characteristic with zero speed. Thus it follows that along each interface and boundary we must specify one interface or boundary condition on w^-, the characteristic variable entering the subdomain. For exterior boundaries, we use the simple boundary condition

$$w^-=Rw^+, \tag{2.5}$$

where R is the reflection coefficient. Choosing $R=-1$ gives a traction-free boundary condition ($\sigma_{iz}n_i=0$), $R=1$ is a rigid wall boundary condition ($v_z=0$), and $R=0$ is a non-reflecting boundary condition. More efficient non-reflective boundary conditions have been developed, e.g., [5, 27], but since the focus of this work is the interface coupling between finite volume and finite difference methods, the simple boundary condition (2.5) is sufficient.

https://doi.org/10.4208/cicp.111013.120914a Published online by Cambridge University Press

The interface condition between two subdomains is expressed as a possibly nonlinear relation of the form

$$w^{-(l)} = \mathcal{W}^{-(l)}\left(w^{+(1)}, w^{+(2)}\right), \quad l = 1, 2, \tag{2.6}$$

where $\mathcal{W}^{-(l)}$ can be different on each side l. Hence the characteristic variables propagating out of the interface are given as a possibly nonlinear combination of those propagating into the interface from both sides.

A special case of (2.6) is the welded interface condition specifying continuity of particle velocities $v_z^{(1)} = v_z^{(2)}$ and tractions acting on the interface $\sigma_{iz}^{(1)} n_i^{(1)} = -\sigma_{iz}^{(2)} n_i^{(2)}$. This results in (2.6) taking the form of continuity of the characteristic variables:

$$w^{-(1)} = -w^{+(2)} \quad \text{and} \quad w^{-(2)} = -w^{+(1)}, \tag{2.7}$$

with the negative sign arising due to the sign convention used in defining the characteristic variables. Along the margins of the plug, the interface condition is taken to be a nonlinear friction law. To express this condition, we first define the slip velocity,

$$V(x,y,t) = v_z^{(2)}(x,y,t) - v_z^{(1)}(x,y,t), \qquad (x, y) \in \gamma, \tag{2.8}$$

as the jump in particle velocity field across the fault (Fig. 2). Force balance requires that the shear tractions $\sigma_{iz}^{(l)} n_i^{(l)}$ exerted on one side (l) by the material on the other side of the fault, be opposite in sign and equal in magnitude:

$$\sigma_{iz}^{(1)}(x,y,t) n_i^{(1)}(x,y) = -\sigma_{iz}^{(2)}(x,y,t) n_i^{(2)}(x,y), \qquad (x, y) \in \gamma. \tag{2.9}$$

These shear tractions are balanced by the frictional resistance to sliding, or shear strength of the fault, $\tau^{(l)}$, that is

$$\tau^{(l)}(x,y,t) = \sigma_{iz}^{(l)}(x,y,t) n_i^{(l)}(x,y), \qquad (x, y) \in \gamma, \tag{2.10}$$

$$n_i^{(1)} = -n_i^{(2)}, \qquad \tau = \tau^{(1)} = -\tau^{(2)}. \tag{2.11}$$

The shear strength τ, which is defined with respect to side (1), is governed by the friction law

$$\tau = F(V,\psi), \qquad \frac{d\psi}{dt} = G(V,\psi), \tag{2.12}$$

where $F(V,\psi)$ is the fault shear strength that depends on the local slip velocity V and an internal state variable ψ that captures the history-dependence of F observed in laboratory experiments. The state variable evolves in time according to a nonlinear ordinary differential equation known as the state evolution law: $d\psi/dt = G(V,\psi)$. The friction coefficient, and hence the shear strength, takes the sign of V (i.e., resistance always opposes the current direction of slip). Explicit forms of $F(V,\psi)$ and $G(V,\psi)$, and further discussion of the nondimensionalization procedure, are given in Appendix B.

https://doi.org/10.4208/cicp.111013.120914a Published online by Cambridge University Press

The existence and uniqueness of the characteristic nonlinear relationship (2.6) satisfying continuity (2.9) using purely velocity-dependent friction laws was analyzed in [35] and extended to a friction law of the form (2.12) in [36]. If $\partial F(V,\psi)/\partial V \leq 0$ then (2.9) and (2.12) can be uniquely expressed as a characteristic relationship of the form (2.6). Additional stability and well-posedness analysis of the antiplane shear problem with a nonlinear boundary condition (but neglecting state evolution) is considered in [47].

2.2 Energy estimate

A suitable definition of well-posedness for our problem is the following:

Definition 2.1. The governing equations (2.1) and (2.2) with homogeneous boundary conditions on exterior boundaries $\partial\Omega$ are said to be well-posed if there exists a unique solution that satisfies the energy rate

$$\frac{d\|\mathbf{q}\|^2}{dt} \leq 0. \tag{2.13}$$

The energy dissipation rate (2.13) ensures that we get an energy estimate and a bounded solution $\mathbf{q}(x,y,t)$ for all times.

In order to obtain an energy estimate we follow [35]. We define the energy using the weighted norm:

$$\|\mathbf{q}\|^2 = \frac{1}{2}\iint_\Omega \left(\mathbf{q}^T\mathbf{q}\right) dxdy = \iint_\Omega \left(\frac{v_z^2}{2} + \frac{\sigma_{iz}\sigma_{iz}}{2}\right) dxdy, \tag{2.14}$$

which is the dimensionless form of the total mechanical energy in the system per unit distance in the $\hat{\mathbf{z}}$-direction. Taking the time derivative of (2.14) and using (2.8)-(2.12) gives

$$\begin{aligned}
\frac{d}{dt}\|\mathbf{q}\|^2 &= \frac{1}{2}\iint_\Omega \mathbf{q}^T\frac{\partial \mathbf{q}}{\partial t}dxdy = \frac{1}{2}\iint_\Omega \mathbf{q}^T(\mathbf{A}_x\frac{\partial \mathbf{q}}{\partial x} + \mathbf{A}_y\frac{\partial \mathbf{q}}{\partial y})dxdy \\
&= \oint_{\partial\Omega} v_z\sigma_{iz}n_i ds + \oint_\gamma v_z^{(1)}\sigma_{iz}^{(1)}n_i^{(1)}ds + \oint_\gamma v_z^{(2)}\sigma_{iz}^{(2)}n_i^{(2)}ds \\
&= \oint_{\partial\Omega} v_z\sigma_{iz}n_i ds + \oint_\gamma v_z^{(1)}\tau^{(1)}ds + \oint_\gamma v_z^{(2)}\tau^{(2)}ds \\
&= \oint_{\partial\Omega} v_z\sigma_{iz}n_i ds - \oint_\gamma VF(V,\psi)ds,
\end{aligned} \tag{2.15}$$

where ds is the infinitesimal arc length of an element of $\partial\Omega$ or γ and the divergence theorem has been used to convert the area integrals to line integrals. To obtain the last term we have used (2.8), (2.10), (2.11), and (2.12). The physical interpretation is straightforward: the total mechanical energy of the system is changed only by work done by tractions on the external boundaries and through dissipation of energy along the internal fault interface during friction sliding.

https://doi.org/10.4208/cicp.111013.120914a Published online by Cambridge University Press

We use the linear characteristic boundary condition (2.5) to show that the exterior boundary terms are nonpositive (i.e., energy can only be lost from the system through these boundaries):

$$\oint_{\partial\Omega} v_z \sigma_{iz} n_i ds = -\frac{1}{4}\oint_{\partial\Omega} (1-R^2)\left(w^+\right)^2 ds \leq 0, \quad \text{if} \quad -1 \leq R \leq 1, \tag{2.16}$$

where (2.4) has been used to convert the physical variables to characteristic variables. On frictional interfaces, energy can only be dissipated. This is guaranteed if

$$VF(V,\psi) \geq 0, \tag{2.17}$$

as universally confirmed by laboratory experiments, which leads to

$$-\oint_{\gamma} VF(V,\psi) ds \leq 0. \tag{2.18}$$

Since both (2.16) and (2.18) are nonpositive it follows that the right hand side of (2.15) is negative semi-definite and we have a energy estimate according to Definition 2.1.

3 Semi-discrete problem

We start off by giving a brief review of the high order finite difference SBP operators in one dimension on an equidistant grid and then move on to finite volume SBP operators in two dimensions on triangular meshes. More details regarding the theory behind SBP operators can be found in e.g., [12, 38, 39, 54, 59, 63].

3.1 High order finite difference method

Consider the field $v(x)$ discretized using a equidistant grid on the unit interval $[0\ 1]$ using $N+1$ grid points:

$$v_i = v(x_i), \qquad x_i = ih, \qquad i = 0,1,\cdots,N, \tag{3.1}$$

where $h = 1/N$ is the grid spacing. An SBP finite difference operator, see [12, 38, 39, 59], satisfies

$$\frac{\partial \mathbf{v}}{\partial x} \approx \mathbf{D}_x \mathbf{v}, \qquad \mathbf{D}_x = \mathbf{P}^{-1}\mathbf{Q}, \tag{3.2}$$

where $\mathbf{v} = [v_0\ v_1\ \cdots\ v_N]^T$ is the grid function (including both interior values and boundary values). The positive definite matrix $\mathbf{P}$ has dimension $(N+1)\times(N+1)$ and defines an inner product that corresponds to the continuous L_2 inner product:

$$(u,v) = \int_0^1 u(x)v(x)dx \quad \text{and} \quad (\mathbf{u},\mathbf{v})_P = \mathbf{u}^T\mathbf{P}\mathbf{v}. \tag{3.3}$$

https://doi.org/10.4208/cicp.111013.120914a Published online by Cambridge University Press

The matrix $\mathbf{Q}$ has dimension $(N+1)\times(N+1)$, it is nearly skew-symmetric and satisfies

$$\mathbf{Q}+\mathbf{Q}^T=\mathbf{diag}[-1\ 0\ \cdots\ 0\ 1]. \tag{3.4}$$

The nearly skew-symmetric property of $\mathbf{Q}$ and discrete inner product property (3.3) have a summation-by-parts property that is analogous to integration-by-parts. Namely,

$$\left(v,\frac{\partial v}{\partial x}\right)=\int_0^1 v\frac{\partial v}{\partial x}dx=\frac{1}{2}\left(v(1)^2-v(0)^2\right),$$
$$(\mathbf{v},\mathbf{D}_x\mathbf{v})_P=\mathbf{v}^T\mathbf{Q}\mathbf{v}=\frac{1}{2}\mathbf{v}^T\left(\mathbf{Q}+\mathbf{Q}^T\right)\mathbf{v}=\frac{1}{2}\left(v_N^2-v_0^2\right),$$

showing why the operators are called summation-by-parts operators.

SBP finite difference operators are constructed by using central difference stencils in the interior and transitioning to one-sided stencils near boundaries. The SBP norm $\mathbf{P}$ can either be diagonal or block diagonal. In this work we consider only the diagonal norm, where the interior stencils have accuracy $q=2s$ ($s=1,\ 2,\cdots$), the boundary stencils have accuracy $r=s$, and global accuracy $p=s+1$ [25,61]. For the specific form of the stencils, see e.g., [12]. When reporting the accuracy of the SBP operators we give the global accuracy.

3.2 Finite volume method

Unstructured SBP operators can be obtained by using a node-centered finite volume method on an unstructured triangular mesh. The finite volume method used here is at most 2^{nd}-order accurate. The finite volume discretization is introduced by partitioning the domain Ω into non-overlapping control volumes Ω_i and solving the governing equations on integral form in each volume. Figs. 3(a)-(b) shows the construction of control volumes. A complete derivation of the finite volume operators is given in [48]. The finite volume approximation to the integral form of the momentum balance equation in (2.1) is written as

$$\mathbf{P}\frac{d\boldsymbol{v}_z}{dt}=\mathbf{Q}_x\boldsymbol{\sigma}_{xz}+\mathbf{Q}_y\boldsymbol{\sigma}_{yz}, \tag{3.5}$$
$$\boldsymbol{v}_z=\left[(v_z)_0\cdots(v_z)_N\right]^T,\quad \boldsymbol{\sigma}_{xz}=\left[(\sigma_{xz})_0\cdots(\sigma_{xz})_N\right]^T,\quad \boldsymbol{\sigma}_{yz}=\left[(\sigma_{yz})_0\cdots(\sigma_{yz})_N\right]^T,$$

where each field value $(v_z)_i$, $(\sigma_{xz})_i$ and $(\sigma_{yz})_i$ is stored at the points $(x_i,\ y_i)$. The remaining governing equations are discretized in a similar manner. In (3.5), the matrix $\mathbf{P}$ stores the area ΔV_i of each control volume Ω_i on the diagonal and defines a discrete inner product that approximates the continuous inner product:

$$(\mathbf{u},\mathbf{v})_P=\mathbf{u}^T\mathbf{P}\mathbf{v}=\sum_{i=0}^{N}\Delta V_i u_i v_i\approx\iint_\Omega uvdxdy. \tag{3.6}$$

https://doi.org/10.4208/cicp.111013.120914a Published online by Cambridge University Press

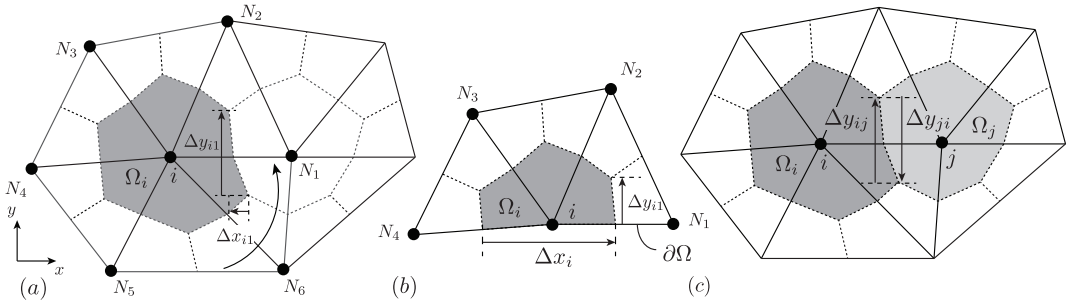


Figure 3: Control volumes (dashed lines) are constructed using midpoints and center of gravities. (a) The control volume Ω_i is constructed around a node i in the interior. The Δx_{ij} and Δy_{ij} are (signed) distances in the $\hat{\mathbf{x}}$-direction and $\hat{\mathbf{y}}$-direction, respectively, each obtained by traversing the control volume boundary in the counterclockwise-direction. (b) On the boundary. (c) Skew-symmetry is preserved in the interior since $\Delta y_{ij} = -\Delta y_{ji}$ for either $i \in \Omega$ or $j \in \Omega$.

The matrices $\mathbf{Q}_x$ and $\mathbf{Q}_y$ are nearly skew-symmetric matrices satisfying

$$(\mathbf{Q}_x)_{ij} = \frac{\Delta y_{ij}}{2} = -(\mathbf{Q}_x)_{ji}, \quad (\mathbf{Q}_y)_{ij} = -\frac{\Delta x_{ij}}{2} = -(\mathbf{Q}_y)_{ji},$$
$$(\mathbf{Q}_x)_{ii} = \begin{cases} 0 & \text{if } i \notin \partial\Omega, \\ \frac{\Delta y_i}{2} & \text{if } i \in \partial\Omega, \end{cases} \quad (\mathbf{Q}_y)_{ii} = \begin{cases} 0 & \text{if } i \notin \partial\Omega, \\ -\frac{\Delta x_i}{2} & \text{if } i \in \partial\Omega, \end{cases} \tag{3.7}$$

where Δx_{ij} and Δy_{ij} are (signed) distances in the $\hat{\mathbf{x}}$- and $\hat{\mathbf{y}}$-directions, respectively, computed by traversing the control volume boundary in the counterclockwise direction, see Fig. 3(a). In Fig. 3(c) we see that $\Delta x_{ij} = -\Delta x_{ji}$ and $\Delta y_{ij} = -\Delta y_{ji}$. It then follows that the matrices

$$\mathbf{X} = \mathbf{Q}_x + \mathbf{Q}_x^T \quad \text{and} \quad \mathbf{Y} = \mathbf{Q}_y + \mathbf{Q}_y^T, \tag{3.8}$$

are diagonal and the only non-zero contribution resides on the boundary, with values $-\Delta x_i$ and Δy_i. We see that the finite volume scheme satisfies the summation-by-parts property:

$$\left(v, \frac{\partial v}{\partial x}\right) = \iint_\Omega v \frac{\partial v}{\partial x} dxdy = \frac{1}{2} \oint_{\partial\Omega} v^2 dy, \quad \left(v, \frac{\partial v}{\partial y}\right) = \iint_\Omega v \frac{\partial v}{\partial y} dxdy = -\frac{1}{2} \oint_{\partial\Omega} v^2 dx,$$
$$(\mathbf{v}, \mathbf{D}_x \mathbf{v})_P = \frac{1}{2} \mathbf{v}^T \mathbf{X} \mathbf{v} = \frac{1}{2} \sum_{i \in \partial\Omega} v_i^2 \Delta y_i, \qquad (\mathbf{v}, \mathbf{D}_y \mathbf{v})_P = \frac{1}{2} \mathbf{v}^T \mathbf{Y} \mathbf{v} = -\frac{1}{2} \sum_{i \in \partial\Omega} v_i^2 \Delta x_i,$$

where Green's theorem has been used to convert area integrals into line integrals.

3.3 Semi-discrete approximations

We partition the computational domain Ω with a nonplanar fault γ in the interior into multiple subdomains as illustrated in Fig. 2(a). In Fig. 2(a), the two subdomains adjacent

https://doi.org/10.4208/cicp.111013.120914a Published online by Cambridge University Press

to the fault are discretized with an unstructured triangular mesh with $N+1$ nodes. All other subdomains are discretized with a structured $(N_x+1)\times(N_y+1)$ Cartesian grid. In the $\hat{\mathbf{x}}$-direction the grid points are separated by the grid spacing h_x and indexed using $i=0,\cdots,N_x$ and in the y-direction they are separated by the grid spacing h_y and indexed using $j=0,\cdots,N_y$. Without loss of generality we assume that each structured grid has the same number of grid points. At every interface the nodes or grid points are collocated.

Considering a subdomain, we formulate a semi-discrete, finite volume approximation to (2.3) (without imposing boundary and interface conditions) as

$$\frac{d\mathbf{q}^{FV}}{dt}=\left[\mathbf{D}_x^{FV}\otimes\mathbf{A}_x\right]\mathbf{q}^{FV}+\left[\mathbf{D}_y^{FV}\otimes\mathbf{A}_y\right]\mathbf{q}^{FV}, \tag{3.9}$$

$$\mathbf{D}_x^{FV}=\mathbf{P}^{-1}\mathbf{Q}_x^{FV},\qquad \mathbf{D}_y^{FV}=\mathbf{P}^{-1}\mathbf{Q}_y^{FV},\qquad \mathbf{q}^{FV}=\begin{bmatrix}\mathbf{q}_0^{FV} & \cdots & \mathbf{q}_N^{FV}\end{bmatrix}^T. \tag{3.10}$$

We have introduced the superscript FV to distinguish the finite volume approximations from the finite difference approximations. The SBP finite volume operators $\mathbf{P}$, $\mathbf{Q_x}^{FV}$, and $\mathbf{Q_y}^{FV}$ are defined in (3.6) and (3.7). The Kronecker product of two matrices is defined as

$$\mathbf{A}\otimes\mathbf{B}=\begin{bmatrix}a_{00}\mathbf{B} & \cdots & a_{0N}\mathbf{B}\\ \vdots & \ddots & \vdots\\ a_{M0}\mathbf{B} & \cdots & a_{MN}\mathbf{B}\end{bmatrix}. \tag{3.11}$$

For the stability analysis we will use the following Kronecker product properties:

$$(\mathbf{A}\otimes\mathbf{B})^T=\mathbf{A}^T\otimes\mathbf{B}^T\quad\text{and}\quad(\mathbf{A}\otimes\mathbf{B})(\mathbf{C}\otimes\mathbf{D})=(\mathbf{AC}\otimes\mathbf{BD}). \tag{3.12}$$

In a similar manner to (3.9), we formulate the semi-discrete, high order finite difference approximation to (2.3) (without imposing boundary and interface conditions) as

$$\frac{d\mathbf{q}^{FD}}{dt}=\left[\mathbf{D}_x^{FD}\otimes\mathbf{A}_x\right]\mathbf{q}^{FD}+\left[\mathbf{D}_y^{FD}\otimes\mathbf{A}_y\right]\mathbf{q}^{FD}, \tag{3.13}$$

$$\mathbf{D}_x^{FD}=\mathbf{P}_x^{-1}\mathbf{Q}_x^{FD}\otimes\mathbf{I}_y,\qquad \mathbf{D}_y^{FD}=\mathbf{I}_x\otimes\mathbf{P}_y^{-1}\mathbf{Q}_y^{FD},$$

$$\mathbf{q}^{FD}=\begin{bmatrix}\mathbf{q}_0^{FD} & \cdots & \mathbf{q}_{N_x}^{FD}\end{bmatrix}^T,\qquad \mathbf{q}_i^{FD}=\begin{bmatrix}\mathbf{q}_{i0}^{FD} & \cdots & \mathbf{q}_{iN_y}^{FD}\end{bmatrix}^T,$$

where q_{ij}^{FD} is the grid function at grid point (x_i^{FD},y_j^{FD}) and $\mathbf{P}_x$, $\mathbf{P}_y$, $\mathbf{Q}_x^{FD}$ and $\mathbf{Q}_y^{FD}$ are the 1-D SBP finite difference operators defined in (3.2), (3.3) and (3.4). The matrices $\mathbf{I}_x$ and $\mathbf{I}_y$ are identity matrices of size $(N_x+1)\times(N_x+1)$ and $(N_y+1)\times(N_y+1)$.

3.4 Boundary conditions and interface conditions

Boundary and interface conditions are imposed weakly using the simultaneous approximation term (SAT) method. In the SAT method, penalty terms are added to the numerical

https://doi.org/10.4208/cicp.111013.120914a Published online by Cambridge University Press

scheme driving the numerical solution towards values satisfying the boundary and interface conditions. Each penalty term corresponds to one boundary. If two (or more) boundaries meet at the same boundary node, then multiple penalty terms are added at that node, thus allowing the method to handle incompatible boundary conditions in a stable manner. Additionally, each penalty term is multiplied with a matrix of penalty weights $\mathbf{\Sigma}$ that are determined for stability.

We now specify penalty terms to impose the welded characteristic interface conditions (2.7), which will couple the finite volume method to the finite difference method. In particular, we treat the case when the north boundary of a finite volume subdomain is coupled to the south boundary of a finite difference domain. We add a penalty term $\mathbf{IT}_N$ to the right hand side of (3.9), as well as a penalty term $\mathbf{IT}_S$ to the right hand side of (3.13). These penalty terms are written as

$$\mathbf{IT}_N = \left(\mathbf{P}^{-1}\mathbf{L}_N \otimes \mathbf{I}_3\right)\mathbf{\Sigma}_N\left[\left(\mathbf{w}_N^- + \mathbf{w}_S^+\right)\otimes \mathbf{e}_3\right], \quad \mathbf{e}_3 = [1\ 1\ 1]^T,$$
$$\mathbf{IT}_S = \left(\mathbf{I}_x \otimes \mathbf{P}_y^{-1} \otimes \mathbf{\Sigma}_S\right)\left[\left(\mathbf{w}_S^- + \mathbf{w}_N^+\right)\otimes \mathbf{e}_S \otimes \mathbf{e}_3\right], \quad \mathbf{e}_S = [1\ 0\ \cdots\ 0]^T.$$

The matrix $\mathbf{L}_N$ is of dimension $(N+1)\times(N_x+1)$ and selects the values from $\mathbf{q}^{FV}$ that are on the north boundary. These boundary values are obtained using $\mathbf{q}_N = (\mathbf{L}_N \otimes \mathbf{I}_3)\mathbf{q}^{FV}$, where $\mathbf{q}_N$ is a vector of size $3(N_x+1)\times 1$ and $\mathbf{I}_3$ is a 3×3 identity matrix. The vector $\mathbf{e}_S$ is of size $(N_y+1)\times 1$ and ensures that the penalty term $\mathbf{IT}_S$ only acts on the south boundary. These boundary values are obtained using $\mathbf{q}_S = \left(\mathbf{I}_x \otimes \mathbf{e}_S^T \otimes \mathbf{I}_3\right)\mathbf{q}^{FD}$. The matrices $\mathbf{\Sigma}_N$ and $\mathbf{\Sigma}_S$ are unknown penalty matrices of dimension $3(l+1)\times 3(l+1)$ and 3×3, respectively, both needed to be determined for stability. We also introduce vectors $(\mathbf{v}_z)_{N/S}$, $(\sigma_{xz})_{N/S}$ and $(\sigma_{yz})_{N/S}$, each of size $3(N_x+1)\times 1$. These vectors are computed from

$$\begin{aligned}
(\mathbf{v}_z)_N &= (\mathbf{L}_N \otimes \mathbf{diag}[1\ 0\ 0])\mathbf{q}^{FV}, & (\mathbf{v}_z)_S &= \left(\mathbf{I}_x \otimes \mathbf{e}_S^T \otimes \mathbf{diag}[1\ 0\ 0]\right)\mathbf{q}^{FD},\\
(\sigma_{xz})_N &= (\mathbf{L}_N \otimes \mathbf{diag}[0\ 1\ 0])\mathbf{q}^{FV}, & (\sigma_{xz})_S &= \left(\mathbf{I}_x \otimes \mathbf{e}_S^T \otimes \mathbf{diag}[0\ 1\ 0]\right)\mathbf{q}^{FD},\\
(\sigma_{yz})_N &= (\mathbf{L}_N \otimes \mathbf{diag}[0\ 0\ 1])\mathbf{q}^{FV}, & (\sigma_{yz})_S &= \left(\mathbf{I}_x \otimes \mathbf{e}_S^T \otimes \mathbf{diag}[0\ 0\ 1]\right)\mathbf{q}^{FD},
\end{aligned} \tag{3.14}$$

where (2.3) has been used. Vectors in the left hand side of these equations are of size $(N_x+1\times 1)$. These vectors are used to compute the characteristics

$$\mathbf{w}_N^{\pm} = (\sigma_{yz})_N \mp (\mathbf{v}_z)_N, \quad \mathbf{w}_S^{\pm} = -(\sigma_{yz})_S \mp (\mathbf{v}_z)_S, \tag{3.15}$$

where (2.1) has been used.

The remaining penalty terms are treated in an analogous manner. For instance, characteristic interface conditions (2.6) are imposed on the fault in the finite volume subdomain by adding

$$\mathbf{FT}^{(k)} = \left[\mathbf{P}^{-1}\mathbf{L}_F^T \otimes \mathbf{I}_3\right]\mathbf{\Sigma}_F^{(k)}\left(\mathbf{w}_F^{-(k)} - \boldsymbol{\mathcal{W}}_F^{(k)}\right)\otimes \mathbf{e}_3, \tag{3.16}$$

https://doi.org/10.4208/cicp.111013.120914a Published online by Cambridge University Press

to the right hand side of (3.9). We use $k=1$, 2 to denote the two sides of the fault. The vector $\boldsymbol{\mathcal{W}}_F^{(k)}$ is of dimension $(l+1)\times 1$, where l is the number of nodes on each side of the fault. This vector is the nonlinear characteristic relationship (2.6), which is derived to satisfy the friction law (2.12). In general, it is not possible to obtain a closed form expression for $\boldsymbol{\mathcal{W}}_F^{(k)}$ due to the nonlinearity of the friction law (2.12). Therefore, we use a bracketed secant method to solve for $\boldsymbol{\mathcal{W}}_F^{(k)}$ [35]. Additionally, we impose the boundary conditions (2.5) on all exterior boundaries, but refer to [35] for details.

3.5 Energy estimate

We define a semi-discrete energy that is analogous to the continuous energy (2.14):

$$\begin{aligned}\|\mathbf{q}(t)\|_P^2 &= \frac{1}{2}\left(\mathbf{q}^{FV}\right)^T(\mathbf{P}\otimes\mathbf{I}_3)\mathbf{q}^{FV}+\frac{1}{2}\left(\mathbf{q}^{FD}\right)^T(\mathbf{P}_x\otimes\mathbf{P}_y\otimes\mathbf{I}_3)\mathbf{q}^{FD}\\ &=\left[\frac{1}{2}\left(\mathbf{v}_z^{FV}\right)^T\mathbf{P}\mathbf{v}_z^{FV}+\frac{1}{2}\left(\boldsymbol{\sigma}_{iz}^{FV}\right)^T\mathbf{P}\boldsymbol{\sigma}_{iz}^{FV}\right]\\ &\quad+\left[\frac{1}{2}\left(\mathbf{v}_z^{FD}\right)^T(\mathbf{P}_x\otimes\mathbf{P}_y)\mathbf{v}_z^{FD}+\frac{1}{2}\left(\boldsymbol{\sigma}_{iz}^{FD}\right)^T(\mathbf{P}_x\otimes\mathbf{P}_y)\boldsymbol{\sigma}_{iz}^{FD}\right].\end{aligned}\tag{3.17}$$

Without loss of generality, we have only defined the energy (3.17) with one finite difference subdomain. In (3.17), the first term is the semi-discrete energy measured in the SBP finite volume norm (3.6) and the second term is the semi-discrete energy measured in the SBP finite difference norm (3.3).

We use the following definition of stability:

Definition 3.1. The semi-discrete formulations (3.13) and (3.9) of the governing equations (2.1) and (2.2) are stable if the energy rate satisfies

$$\frac{d\|\mathbf{q}(t)\|_P^2}{dt}\leq 0.\tag{3.18}$$

This definition of stability is consistent with Definition 2.1 of well-posedness. For more general definitions of stability, see for example [26].

By taking the time derivative of (3.17) we get the energy rate

$$\frac{d}{dt}\|\mathbf{q}(t)\|_P^2 = BT+FT+IT,\tag{3.19}$$

where we substituted $d\mathbf{q}^{FV}/dt$ and $d\mathbf{q}^{FD}/dt$ into (3.9), or (3.13), and used the nearly-skew symmetric properties (3.4) and (3.8) of the SBP operators. The terms BT, FT, and IT are the semi-discrete energy rate contributions from all exterior boundaries, faults and interfaces. The penalty matrices Σ in each term BT, FT, and IT will be chosen such that these terms become negative semi-definite. We will ignore BT, since the treatment of exterior boundaries can be found in [35].

https://doi.org/10.4208/cicp.111013.120914a Published online by Cambridge University Press

3.6 Hybrid interface treatment

We begin by considering the energy rate contribution from the interface term IT in (3.19). Here we exclusively consider the hybrid interface; treatment of the structured-structured interface can be found in [35], see also [12, 13, 24]. The hybrid interface treatment in this section follows the path set in [23, 49, 52]. Since all the hybrid interfaces are handled in a similar manner, we exclusively consider the interface between the north boundary of a finite volume subdomain and the south boundary of a finite difference subdomain. The interface terms are

$$\begin{aligned} IT = IT_N + IT_S = & \frac{1}{2}\mathbf{q}_N^T(\mathbf{Y}_N \otimes \mathbf{A}_y)\mathbf{q}_N + \mathbf{q}_N\boldsymbol{\Sigma}_N\left[(\mathbf{w}_N^- + \mathbf{w}_S^+)\otimes \mathbf{e}_3\right] \\ & + \frac{1}{2}\mathbf{q}_S(\mathbf{P}_x \otimes \mathbf{E}_S \otimes \mathbf{A}_y)\mathbf{q}_S + \mathbf{q}_S(\mathbf{P}_x \otimes \mathbf{E}_S \otimes \boldsymbol{\Sigma}_S)\left[(\mathbf{w}_S^- + \mathbf{w}_N^+)\otimes \mathbf{e}_3\right] \\ = & (\mathbf{v}_z)_N^T \mathbf{Y}_N (\sigma_{yz})_N - (\mathbf{v}_z)_S^T \mathbf{P}_x (\sigma_{yz})_S \\ & + \left(\boldsymbol{\Sigma}_{N1}(\mathbf{v}_z)_N + \boldsymbol{\Sigma}_{N2}(\sigma_{xz})_N + \boldsymbol{\Sigma}_{N3}(\sigma_{yz})_N\right)^T (\mathbf{w}_N^- + \mathbf{w}_S^+) \\ & + \left(\Sigma_{S1}(\mathbf{v}_z)_S + \Sigma_{S2}(\sigma_{xz})_S + \Sigma_{S3}(\sigma_{yz})_S\right)^T \mathbf{P}_x(\mathbf{w}_S^- + \mathbf{w}_N^+). \end{aligned} \tag{3.20}$$

In (3.20), we have used (2.3) to replace $\mathbf{q}_{N/S}$ with $(\mathbf{v}_z)_{N/S}$, $(\sigma_{xz})_{N/S}$, and $(\sigma_{yz})_{N/S}$. The matrix $\mathbf{Y}_N$ is a $(N_x+1)\times(N_x+1)$ diagonal matrix containing the values of $\mathbf{Y}$ belonging to the north boundary and it can be computed using $\mathbf{Y}_N = \mathbf{L}_N\mathbf{Y}\mathbf{L}_N^T$, where $\mathbf{L}_N$ is of dimension $(N_x+1)\times(N+1)$ (see Section 3.4). We have also introduced $\mathbf{E}_S = \mathbf{diag}[\mathbf{e}_S]$. The penalty matrices are defined as $\boldsymbol{\Sigma}_N = \mathbf{diag}[1\ 0\ 0]\otimes\boldsymbol{\Sigma}_{N1} + \mathbf{diag}[0\ 1\ 0]\otimes\boldsymbol{\Sigma}_{N2} + \mathbf{diag}[0\ 0\ 1]\otimes\boldsymbol{\Sigma}_{N3}$ and $\boldsymbol{\Sigma}_S = \mathbf{diag}[\Sigma_{S1}\ \Sigma_{S1}\ \Sigma_{S3}]$. Choosing $\boldsymbol{\Sigma}_{N1} = \boldsymbol{\Sigma}_{N3} = -\mathbf{Y}_N/2$, $\boldsymbol{\Sigma}_{N2} = \mathbf{0}$, $\Sigma_{S1} = -\Sigma_{S3} = -1/2$ and $\Sigma_{S2} = 0$, leads to

$$\begin{aligned} IT_N + IT_S = & (\mathbf{v}_z)_N^T \mathbf{Y}_N (\sigma_{yz})_N - (\mathbf{v}_z)_S^T \mathbf{P}_x (\sigma_{yz})_S \\ & - \frac{1}{2}\left((\sigma_{yz})_N + (\mathbf{v}_z)_N\right)^T \mathbf{Y}_N (\mathbf{w}_N^- + \mathbf{w}_S^+) \\ & - \frac{1}{2}\left(-(\sigma_{yz})_S + (\mathbf{v}_z)_S\right)^T \mathbf{P}_x (\mathbf{w}_S^- + \mathbf{w}_N^+) \\ = & -\frac{1}{4}\Big((\mathbf{w}_N^+ + \mathbf{w}_S^+)^T \mathbf{Y}_N (\mathbf{w}_N^+ - \mathbf{w}_S^+) \\ & + (\mathbf{w}_S^+ + \mathbf{w}_N^+)^T \mathbf{P}_x (\mathbf{w}_S^+ - \mathbf{w}_N^+) \\ & + (\mathbf{w}_N^- + \mathbf{w}_S^+)^T \mathbf{Y}_N (\mathbf{w}_N^- + \mathbf{w}_S^+) \\ & + (\mathbf{w}_S^- + \mathbf{w}_N^+)^T \mathbf{P}_x (\mathbf{w}_S^- + \mathbf{w}_N^+)\Big). \end{aligned} \tag{3.21}$$

In (3.21), we have used (3.15) to replace $(\mathbf{v}_z)_{N/S}$, $(\sigma_{xz})_{N/S}$, and $(\sigma_{yz})_{N/S}$ with $\mathbf{w}_{N/S}^{\pm}$. The SBP operator $\mathbf{P}_x$ is positive definite and $\mathbf{Y}_N = -\mathbf{diag}[\Delta x_i]$ for Δx_i belonging to the north boundary. Recall that Δx_i is a signed distance quantity obtained by traversing the north boundary in the counter-clockwise direction. Traversal of this boundary is

https://doi.org/10.4208/cicp.111013.120914a Published online by Cambridge University Press

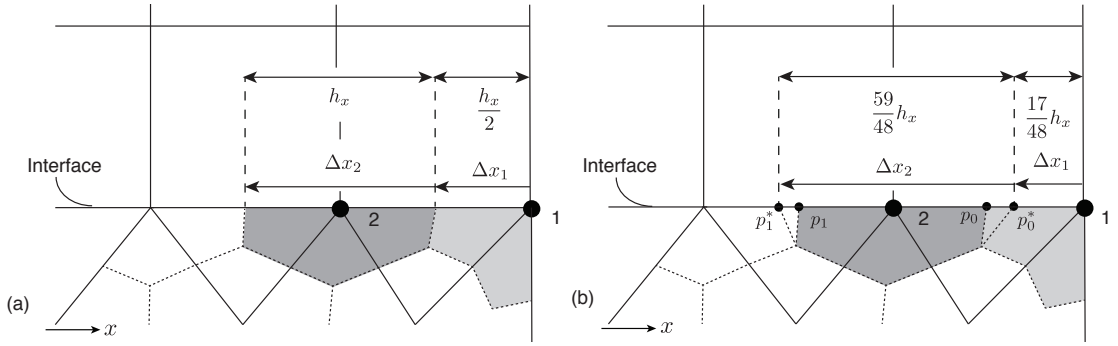


Figure 4: Hybrid interface treatment. (a) The second-order SBP finite difference operator $\mathbf{P}_x$ matches the SBP finite volume operator $\mathbf{Y}_N = -\mathbf{diag}[\Delta x_i]$. (b) The fourth-order SBP finite difference method has $\mathbf{P}_x = h_x\mathbf{diag}[17/48\ 59/48\ 43/48\ 49/48\ 1\ \cdots\ 1\ 49/48\ 43/48\ 59/48\ 17/48]$ which is incompatible with the standard formulation of $\mathbf{Y}_N$. To ensure $\mathbf{P}_x = \mathbf{Y}_N$, the finite volume operators $\mathbf{Q}_x$ and $\mathbf{Q}_y$ are modified by repositioning some of the nodes in the dual mesh located on the hybrid interfaces. In the example shown, the nodes at p_0 and p_1 are moved to p_0^* and p_1^*, respectively.

in the negative $\hat{\mathbf{x}}$-direction and therefore $\Delta x_i < 0$ (see Fig. 4(a)). From this it follows that $-\left(\mathbf{w}_S^+\right)^T\mathbf{Y}_N\mathbf{w}_S^+$ and $-\left(\mathbf{w}_N^+\right)^T\mathbf{P}_x\mathbf{w}_N^+$ in (3.21) are non-positive. Therefore, stability follows if $\mathbf{Y}_N = \mathbf{P}_x$ [49,52]. With this assumption, Eq. (3.21) becomes

$$IT_N + IT_S = -\frac{1}{4}\Big(\left(\mathbf{w}_N^- + \mathbf{w}_S^+\right)^T\mathbf{P}_x\left(\mathbf{w}_N^- + \mathbf{w}_S^+\right) + \left(\mathbf{w}_S^- + \mathbf{w}_N^+\right)^T\mathbf{P}_x\left(\mathbf{w}_S^- + \mathbf{w}_N^+\right)\Big) \leq 0. \tag{3.22}$$

The estimate (3.22) proves stability of the hybrid interface treatment. There is no energy dissipation in the volume of the continuous problem, thus this energy dissipation at the hybrid interface is a numerical result. That said, the rate of energy dissipation decreases with mesh refinement as $\mathbf{w}_N^-$ converges to $\mathbf{w}_S^+$.

For the 2^{nd}-order SBP finite difference method, $\mathbf{P}_x$ is equivalent to $\mathbf{Y}_N$. This follows from the fact that the grid spacing on the interface is equidistant and the points on the interface are collocated as shown in Fig. 4(a). For all higher order SBP finite difference methods $\mathbf{P}_x$ and $\mathbf{Y}_N$ do not match. To satisfy $\mathbf{P}_x = \mathbf{Y}_N$ for the higher order methods the control volumes along the hybrid interface must be slightly modified; see Fig. 4(b) and [23,49,52] for more details.

3.7 Fault interface treatment

Without loss of generality we only consider a single, smooth fault γ. The same procedure as for the hybrid interface treatment leads to

$$FT = \sum_{k=1}^{2}\left[\frac{1}{2}\left(\mathbf{q}_F^{(k)}\right)^T\left(\mathbf{X}_F\otimes\mathbf{A}_x + \mathbf{Y}_F\otimes\mathbf{A}_y\right)\mathbf{q}_F^{(k)} + \left(\mathbf{q}_F^{(k)}\right)^T\mathbf{\Sigma}_F^{(k)}\left(\left(\mathbf{w}_F^{-(k)} - \boldsymbol{\mathcal{W}}_F^{-(k)}\right)\otimes\mathbf{e}_3\right)\right]$$

https://doi.org/10.4208/cicp.111013.120914a Published online by Cambridge University Press

$$=\sum_{k=1}^{2}\Bigg[\left(\mathbf{v}_z^{(k)}\right)_F^T\mathbf{X}_F^{(k)}\left(\sigma_{xz}^{(k)}\right)_F+\left(\mathbf{v}_z^{(k)}\right)_F^T\mathbf{Y}_F^{(k)}\left(\sigma_{yz}^{(k)}\right)_F$$
$$+\left(\mathbf{\Sigma}_{F1}^{(k)}\left(\mathbf{v}_z^{(k)}\right)_F+\mathbf{\Sigma}_{F2}^{(k)}\left(\sigma_{xz}^{(k)}\right)_F+\mathbf{\Sigma}_{F3}^{(k)}\left(\sigma_{yz}^{(k)}\right)_F\right)^T\left(\mathbf{w}_F^{-(k)}-\boldsymbol{\mathcal{W}}_F^{(k)}\right)\Bigg],$$

where $\mathbf{q}_F^{(k)}$ contains the values of $\mathbf{q}^{FV}$ on side (k) of the fault. Furthermore, we have defined $\mathbf{X}_F^{(k)}=(\mathbf{L_F}^{(k)})^T\mathbf{X}\mathbf{L}_F^{(k)}$ and $\mathbf{Y}_F^{(k)}=(\mathbf{L_F}^{(k)})^T\mathbf{Y}\mathbf{L}_F^{(k)}$, where $\mathbf{L}_F^{(k)}$ is of dimension $l\times(N+1)$ with l number of nodes on each side of the fault (see Section 3.4). Choosing the penalty terms $\mathbf{\Sigma}_{F1}^{(k)}=-\mathbf{S}_F/2$, $\mathbf{\Sigma}_{F2}^{(k)}=-\mathbf{X}_F^{(k)}/2$ and $\mathbf{\Sigma}_{F3}^{(k)}=-\mathbf{Y}_F^{(k)}/2$ leads to

$$FT=-\left(\hat{\mathbf{V}}\right)^T\mathbf{S}_F\mathbf{F}(\hat{\mathbf{V}},\boldsymbol{\psi})-\frac{1}{4}\sum_{k=1}^{2}\left(\mathbf{w}_F^{-(k)}-\boldsymbol{\mathcal{W}}_F^{-(k)}\right)^T\mathbf{S}_F\left(\mathbf{w}_F^{-(k)}-\boldsymbol{\mathcal{W}}_F^{-(k)}\right),\tag{3.23}$$

where $\hat{\mathbf{V}}$ and $\mathbf{S}_F$ are defined in Appendix B, including additional derivation steps. Since $\mathbf{F}(\hat{\mathbf{V}},\boldsymbol{\psi})$ is the same as in the continuous problem and $\mathbf{S}_F$ is positive definite, it follows from (2.17) that $\left(\hat{\mathbf{V}}\right)^T\mathbf{S}_F\mathbf{F}(\hat{\mathbf{V}},\boldsymbol{\psi})\geq 0$ and energy is dissipated at the fault. The others terms are also non-positive and, consequently $FT\leq 0$, which proves stability for the fault interface treatment.

4 Stability, convergence and efficiency

In this section, we consider the stability and accuracy of the hybrid method using numerical experiments. Since this paper deals with the practical use of a well-defined and provably stable method, we refer the reader to previous work for more theoretical details [23, 48–50, 52]. To investigate the efficiency of the hybrid method we also compare with the use of the finite volume method for the entire domain.

Because there are no known closed form solutions to the governing equations (2.3) and friction law (2.12) for complex fault geometries, we use the method of manufactured solutions [57]. With this approach, the original problem is modified by adding source terms to the governing equations, interface conditions, and boundary conditions such that the modified problem satisfies a solution known a priori. The manufactured solution we have used is presented in Appendix C.

The error is measured using $\|\mathbf{e}\|_P=\|\mathbf{q}-\mathbf{q}^*\|_P$, where the norm is the nondimensionalized energy (3.17), $\mathbf{q}=\left[\mathbf{v}_z,\,\sigma_{xz},\,\sigma_{yz}\right]^T$ is the numerical solution, and $\mathbf{q}^*$ is the manufactured solution. The manufactured solution $\boldsymbol{q}^*$ is computed using (C.5).

The computational domain Ω is a square of nondimensional size $L_x\times L_y=7.2\times 7.2$, containing a circular fault of radius $R=0.6$ centered at the origin. We perform computations using hybrid meshes (see Fig. 5) with increasing refinement. Each hybrid mesh is denoted by $j=1,\,2,\cdots$, where $j=1$ corresponds to the coarsest mesh (no refinement

https://doi.org/10.4208/cicp.111013.120914a Published online by Cambridge University Press

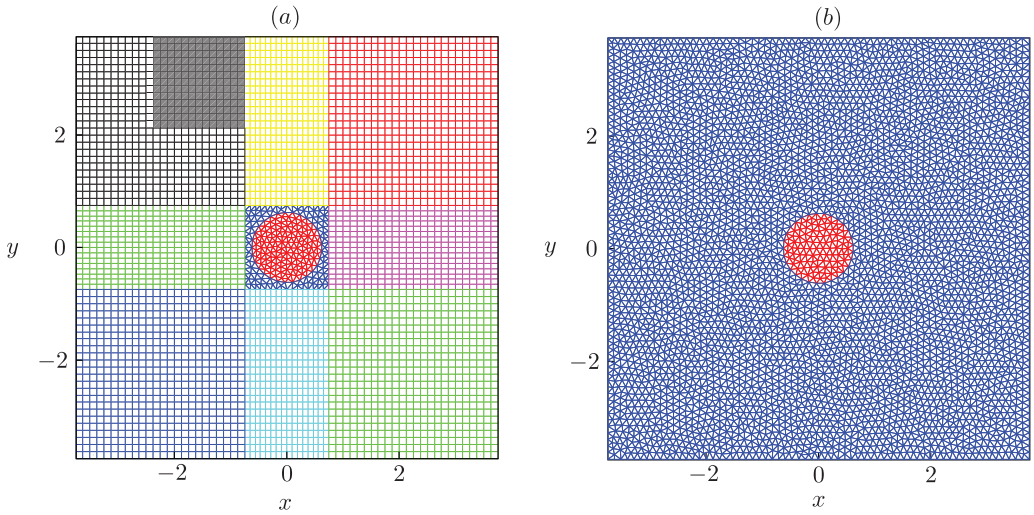


Figure 5: (a) Circular plug geometry meshed with a hybrid mesh consisting of 2 unstructured meshes and 8 structured grids. Far field error is measured in the shaded region. (b) Circular plug geometry meshed with 2 unstructured meshes.

applied). For each refinement the mesh resolution is increased nearly uniformly everywhere. The number of triangular elements in the unstructured meshes increases approximately by a factor of 4 for each refinement. In each of the structured grids, identical grid spacing is used in both directions ($h_x = h_y$), and this grid spacing is decreased by half for each refinement. On the hybrid interfaces all nodes are inserted equidistantly with $2^{j+4}+1$ points on each boundary. Furthermore, on each side of the fault boundary 30×2^j nodes are inserted equidistantly. The circular fault is approximated using piecewise linear segments. As the mesh is refined, new boundary nodes are added to conform to the shape of the fault with equidistant grid spacing.

We use the 2^{nd}-order finite volume method on the unstructured mesh and the 2^{nd}-, 3^{rd}-, and 4^{th}-order finite difference method on the structured grids. Recall that the 4^{th}-order finite difference method achieves 4^{th}-order global accuracy when it is not coupled to the finite volume method. The final time is taken to be $T = 640$, which corresponds to 400 oscillations of the solution. Time integration is carried out using the 4^{th}-order low storage Runge-Kutta scheme by Carpenter and Kennedy [11]. The time step is $\Delta t = 0.35 h_{\min}$, where the parameter $h_{\min}$ is the minimum length of an edge in the hybrid mesh. We study the error in time for meshes $j = 1$, 2,3. The results obtained using 3^{rd}- and 4^{th}-order SBP finite difference operators are reported in Figs. 6(a) and 6(b), respectively. Both Fig. 6(a) and Fig. 6(b) show that the error measured in the energy norm remains bounded, thus confirming stability and an error bound, see [46]. There is no significant difference in accuracy between the 3^{rd}- and 4^{th}-order SBP finite difference operators. Although not shown here, stability was also confirmed using the 2^{nd}-order SBP finite difference operators.

https://doi.org/10.4208/cicp.111013.120914a Published online by Cambridge University Press

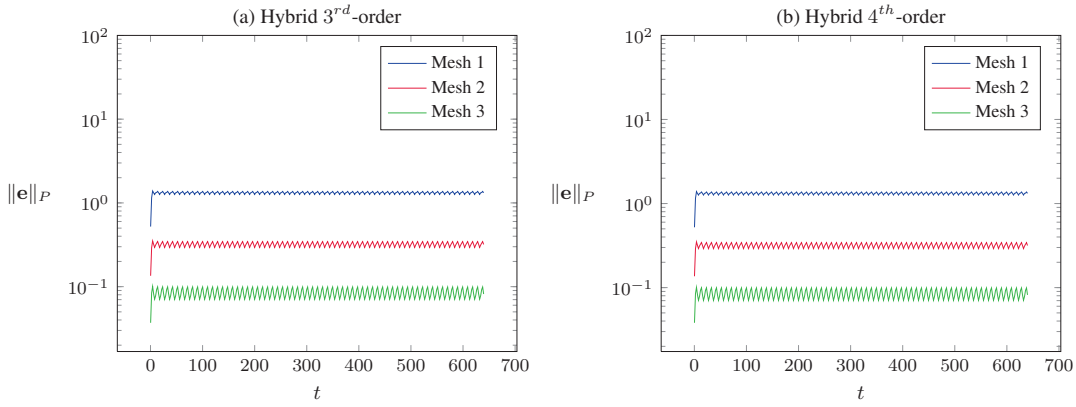


Figure 6: Error in the energy norm on the first three hybrid meshes listed in Table 1. No error growth in time. (a) Hybrid method using 3^{rd}-order SBP finite difference operators. (b) Hybrid method using 4^{th}-order SBP finite difference operators.

The accuracy of the hybrid method is compared to the accuracy of the pure finite volume method. In order to perform this comparison, we mesh the entire computational domain with an unstructured mesh. The mesh quality and element size of this mesh is constructed similarly to the smaller, unstructured mesh used by the hybrid method. For both methods, the convergence rate is estimated using

$$\frac{\log_{10}\left(\|\mathbf{e}_j\|_P/\|\mathbf{e}_{j+1}\|_P\right)}{\log_{10}\left(\sqrt{N_j}/\sqrt{N_{j+1}}\right)}, \tag{4.1}$$

where $\|\mathbf{e}_j\|_P$ is the error measured on mesh j, using N_j number of nodes. For the hybrid meshes, the number of nodes is the sum of all nodes in the unstructured meshes and structured grids. Fig. 7 shows convergence for both the pure finite volume method and

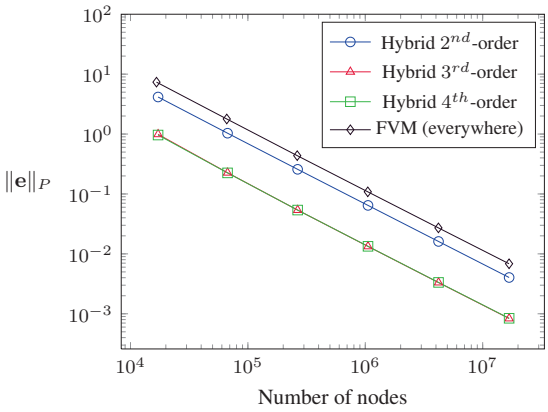


Figure 7: Convergence of the hybrid method and finite volume method applied everywhere. There is no gain in accuracy from using the hybrid method with more than 3^{rd}- and 4^{th}-order SBP finite difference operators.

https://doi.org/10.4208/cicp.111013.120914a Published online by Cambridge University Press

Table 1: Error and convergence rates using the hybrid method with 2^{nd}-, 3^{rd}-, and 4^{th}-order SBP finite difference operators.

	Hybrid 2^{nd}-order		Hybrid 3^{rd}-order		Hybrid 4^{th}-order	
Nodes	Error	Rate	Error	Rate	Error	Rate
1.72×10^{4}	4.15×10^{0}		9.90×10^{-1}		9.63×10^{-1}	
6.71×10^{4}	1.03×10^{0}	2.04×10^{0}	2.26×10^{-1}	2.17×10^{0}	2.25×10^{-1}	2.13×10^{0}
2.65×10^{5}	2.58×10^{-1}	2.02×10^{0}	5.38×10^{-2}	2.09×10^{0}	5.39×10^{-2}	2.08×10^{0}
1.05×10^{6}	6.44×10^{-2}	2.01×10^{0}	1.33×10^{-2}	2.02×10^{0}	1.34×10^{-2}	2.02×10^{0}
4.21×10^{6}	1.61×10^{-2}	2.00×10^{0}	3.32×10^{-3}	2.01×10^{0}	3.34×10^{-3}	2.01×10^{0}
1.68×10^{7}	4.03×10^{-3}	2.00×10^{0}	8.34×10^{-4}	2.00×10^{0}	8.41×10^{-4}	1.99×10^{0}

Table 2: Error and convergence rates using the finite volume method (FVM) applied in the entire computational domain.

FVM (everywhere)		
Nodes	Error	Rate
1.67×10^{4}	7.35×10^{0}	
6.61×10^{4}	1.78×10^{0}	2.05×10^{0}
2.63×10^{5}	4.36×10^{-1}	2.04×10^{0}
1.05×10^{6}	1.09×10^{-1}	2.01×10^{0}
4.20×10^{6}	2.72×10^{-2}	2.00×10^{0}
1.68×10^{7}	6.84×10^{-3}	1.99×10^{0}

the hybrid method at $T=3.2$. The error for the hybrid method calculations are listed in Table 1 and the pure finite volume method in Table 2. The hybrid method is at most 2^{nd}-order accurate. This order of accuracy is expected because the global order of accuracy of the coupled SBP methods cannot exceed the order of accuracy of the method with the lowest order of accuracy [61]. Additionally, in this test, there is no benefit in terms of the overall global error from using the 4^{th}-order SBP finite difference operators, though there is an order of magnitude accuracy gain from using the 3^{rd}-order instead of the 2^{nd}-order SBP finite difference operators.

We next investigate the error in the far field. Consider the region $[-2.3\ -0.7]\times[2.0\ 3.6]$ in the north-west quadrant of the computational domain (shaded region in Fig. 5). Fig. 8(a) shows the error in this region using the hybrid method with 2^{nd}-, 3^{rd}-, and 4^{th}-order SBP finite difference operators on the finest mesh ($j=6$). The initial accuracy of the hybrid method with 3^{rd}- and 4^{th}-order SBP finite difference operators is eventually lost. Loss in accuracy occurs when the truncation error generated in the near field has propagated and polluted the solution in the far field. We compute the convergence rates in the far field at time $t_0=0.8$, which is before the error generated in the near field has reached the far field. Fig. 8(b) and Table 3 show the convergence rates at this time. These convergence

https://doi.org/10.4208/cicp.111013.120914a Published online by Cambridge University Press

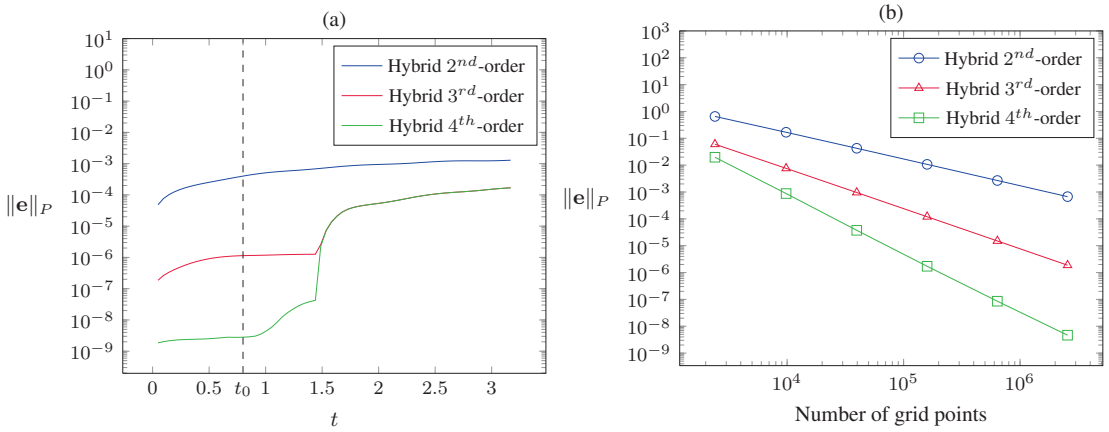


Figure 8: Error measured in the far field on one structured grid (shaded in region in Fig. 5). (a) Error originating from the near field propagates into the far field and pollutes the solution, limiting convergence rate. (b) Convergence in the far field at $t_0=0.8$ (before the error from the near field has reached the far field). Table 3 lists convergence rates. The 2^{nd}-, 3^{rd}-, and 4^{th}-order SBP finite difference operators are used in the hybrid method.

Table 3: Error and convergence rates in the far field on one structured grid (shaded region in Fig. 5) at time $t_0=0.8$. Convergence rates are in agreement with theoretical convergence rates for pure SBP high order finite difference schemes.

	Hybrid 2^{nd}-order		Hybrid 3^{rd}-order		Hybrid 4^{th}-order	
Grid points	Error	Rate	Error	Rate	Error	Rate
$2.40\cdot10^{3}$	$6.53\cdot10^{-1}$		$6.02\cdot10^{-2}$		$1.97\cdot10^{-2}$	
$9.80\cdot10^{3}$	$1.68\cdot10^{-1}$	1.93	$7.61\cdot10^{-3}$	2.94	$8.78\cdot10^{-4}$	4.42
$3.96\cdot10^{4}$	$4.26\cdot10^{-2}$	1.97	$9.58\cdot10^{-4}$	2.97	$3.75\cdot10^{-5}$	4.52
$1.59\cdot10^{5}$	$1.07\cdot10^{-2}$	1.98	$1.20\cdot10^{-4}$	2.98	$1.72\cdot10^{-6}$	4.43
$6.38\cdot10^{5}$	$2.69\cdot10^{-3}$	1.99	$1.50\cdot10^{-5}$	2.99	$8.57\cdot10^{-8}$	4.31
$2.56\cdot10^{6}$	$6.73\cdot10^{-4}$	2.00	$1.88\cdot10^{-6}$	3.00	$4.64\cdot10^{-9}$	4.20

rates are in agreement with the theoretical convergence rates of the SBP finite difference operators.

The efficiency of the hybrid methods is improved by coarsening the structured grids without exceeding the pure finite volume method errors. Since the grid points on the hybrid interfaces must be collocated, only grid points along lines that are normal to the hybrid interfaces are removed. This increases the grid spacing from h_0 to h_n. Table 4 shows the maximum grid stretching h_n/h_0 that gave errors matching the pure finite volume method errors shown in Table 2, for the meshes $j=1,\cdots,4$. On mesh $j=4$, the maximum grid stretching with the hybrid method using the 4^{th}-order SBP finite difference operators is a factor of ~ 1.4 larger than the hybrid method using the 3^{rd}-order SBP finite difference operators, thus showing the advantage of using the 4^{th}-order SBP finite difference operators.

https://doi.org/10.4208/cicp.111013.120914a Published online by Cambridge University Press

Table 4: Hybrid methods with coarsened grids. The maximum grid stretching h_0/h_n is determined by coarsening the grids until the error nearly matches the pure finite volume method error (cf. errors on meshes $j=1,\cdots,4$, in Table 2).

Hybrid 2^{nd}-order			Hybrid 3^{rd}-order			Hybrid 4^{th}-order		
Nodes	h_n/h_0	Error	Nodes	h_n/h_0	Error	Nodes	h_n/h_0	Error
1.67×10^4	1.36×10^0	6.56×10^0	4.78×10^3	3.76×10^0	7.26×10^0	5.35×10^3	3.37×10^0	4.79×10^0
6.08×10^4	1.44×10^0	1.77×10^0	1.49×10^4	4.74×10^0	1.53×10^0	1.39×10^4	5.12×10^0	1.50×10^0
2.47×10^5	1.41×10^0	4.28×10^{-1}	4.64×10^4	6.24×10^0	3.98×10^{-1}	4.13×10^4	7.31×10^0	3.50×10^{-1}
9.91×10^5	1.41×10^0	1.06×10^{-1}	1.52×10^5	8.13×10^0	1.04×10^{-1}	1.27×10^5	1.09×10^1	9.12×10^{-2}

5 Abrupt sliding plug in volcanic conduit

Having verified stability and accuracy of our hybrid method, we now apply it to the problem of volcanic earthquakes. Throughout this section all variables and parameters are dimensional.

Regularly repeating earthquakes were observed during the 2004-2008 eruption of Mount Saint Helens, Washington, and were attributed to unstable frictional sliding along the margins of a crystalline plug being extruded from the top of the volcano [31,45]. The plug is pushed upward by pressure acting on its base and pulled down by its weight and frictional forces along the interface between the plug and surrounding conduit walls. In the model proposed in [31], pressure at the base of the plug increases due to a steady influx of compressible magma beneath it. When the frictional resistance and gravity can no longer accommodate the increasing pressure, abrupt sliding commences. Rapid slip excites seismic waves that are radiated outward into the surrounding host rock. Upward movement of the plug decompresses the magma column beneath it and ultimately stops sliding. The simplified model in [31] successfully explained the size and periodicity of the drumbeat earthquakes, but made no predictions of seismic waveforms.

We demonstrate how the model can be expanded upon by using our hybrid method to simulate the dynamics of a single drumbeat earthquake event. We focus on the initial waves associated with the onset of unstable slip, allowing us to neglect the decompression of the magma that ultimately bounds slip. With this approximation, events in our model, once nucleated, never stop.

Initially, the plug and surrounding material are assumed to be at rest. A uniform shear stress τ_0 acts on the margins of the plug. The initial conditions, material properties, and other parameters are given and explained in Table 5. The frictional parameters a and b are chosen such that the fault is velocity-weakening in steady state (i.e., $b-a>0$). Prior to sliding when accelerations are negligible, all forces acting on the plug must balance. For a plug with constant radius R the force balance is

$$\pi R^2 p - 2\pi R H \tau_0 - \pi R^2 H \rho g = 0, \tag{5.1}$$

assuming a constant vertical extent H of the plug. In addition, p is the pressure exerted

https://doi.org/10.4208/cicp.111013.120914a Published online by Cambridge University Press

Table 5: Material properties and physical parameters.

	Parameter	Symbol	Value
Material Properties			
	Shear wavespeed	c	3.3 km/s
	Shear modulus	G	30 GPa
Friction-Law Parameters			
	Direct effect parameter	a	0.01
	Evolution effect parameter	b	0.014
	Reference slip velocity	V_0	1 μm/s
	Reference friction coefficient	f_0	0.6
	State-evolution distance	L	0.3 mm
Pressure Perturbation Parameters			
	Amplitude	A	5 MPa
	Width	W	2 m
	Relaxation time	t_0	0.1 ms^{-1}
	X-coordinate	x_0	0 m
	Y-coordinate	y_0	42.5 m
Initial Conditions			
	Normal stress on the plug margin	σ_0	27 MPa
	Shear stress on the plug margin	τ_0	15.5 MPa
	Initial state variable	ψ_0	0.54

on the base of the plug and g is the gravitational acceleration. Solving (5.1) for τ_0 yields

$$\tau_0 = \frac{R}{2}\left(\frac{p}{H} - \rho g\right). \tag{5.2}$$

For our purposes we take p to be constant. In a more realistic model, upward motion of the plug would decompress the magma beneath it, thereby reducing p.

To illustrate the capabilities of our method, we consider the non-cylindrical plug shape shown in Fig. 1. Specifically, we allow the radius R to vary with angle θ according to

$$\begin{aligned} R(\theta) = {} & 45\text{ m} + 12\text{ m}\times\sin(\theta) + 2.25\text{ m}\times\sin(\theta-\pi/4) + 0.75\text{ m}\times\sin(6\theta+\pi) \\ & - 1.8\text{ m}\times\cos(12\theta+\pi/3) + 10.5\text{ m}\times\cos(1.2\theta). \end{aligned} \tag{5.3}$$

The geometry is meshed with a hybrid mesh similar to the MMS problem in Section 4 (see Fig. 5).

https://doi.org/10.4208/cicp.111013.120914a Published online by Cambridge University Press

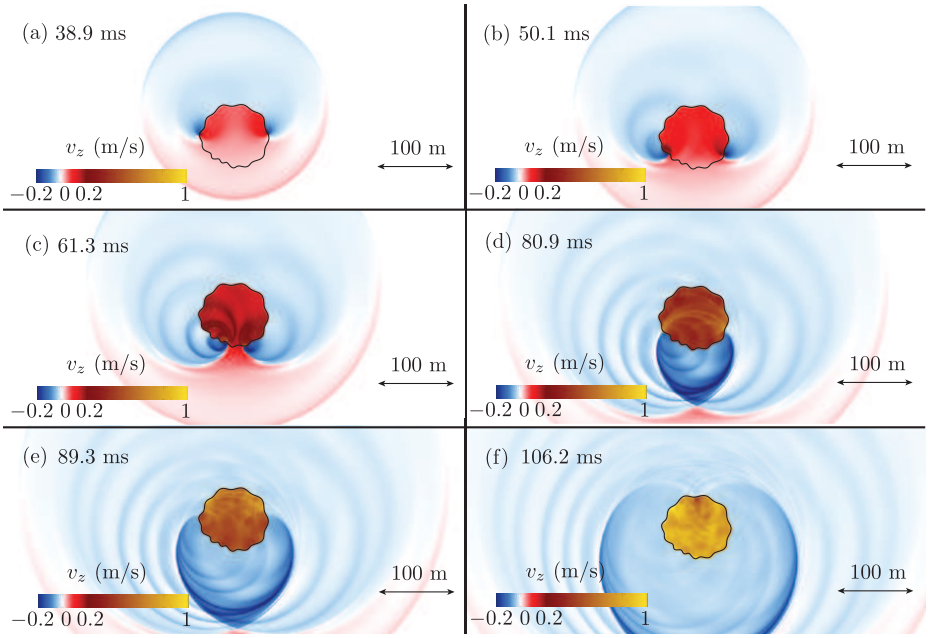


Figure 9: Seismic wave field excited by the propagating rupture. Trapping and wave focusing occurs in the plug.

To initiate the event, we artificially increase the initial shear stress in a small, localized patch along the margins of the plug over the rise time t_0. If the width W and amplitude A of the perturbation is sufficiently large, then the unstable slip commences and triggers progressive failure of neighboring parts of the fault. Rupture nucleation takes place at the most northern position on the plug margin. The nucleation depth is approximately 1 km below the surface, where we estimate the normal stress to be approximately $\sigma_0 = 27$ MPa.

We run the simulation for $T = 120$ ms using the 4^{th}-order SBP finite difference operators. Initially the plug is motionless. Sliding commences abruptly over a small section along the plug margin. Wave-mediated stress transfer to adjacent parts of the fault initiate sliding there and the rupture spreads outward, at a speed determined by the elastic waves, in both directions. Initial particle velocities are nearly identical in magnitude inside and outside the plug. Geometrical complexities in the plug margin profile cause the rupture to accelerate and decelerate, exciting bursts of waves that appear in the wavefield snapshots shown in Fig. 9. The evolution and nonlinearity of the frictional interface conditions can also be seen in that figure: waves incident upon the sections of the fault prior to rupture are transmitted (Fig. 9(a) or Fig. 9(b)). Upon rupture the slipping fault assumes a more reflective nature, and incident waves crossing the plug are reflected and focused inward (Fig. 9(e) and Fig. 9(f)). This trapping of waves within the plug is unique to this fault geometry and ultimately causes particle velocities in the plug to be nearly an order of magnitude larger than those in the surrounding material. This challenging application problem, involving nonlinear evolution of interface conditions driven by wave focusing,

https://doi.org/10.4208/cicp.111013.120914a Published online by Cambridge University Press

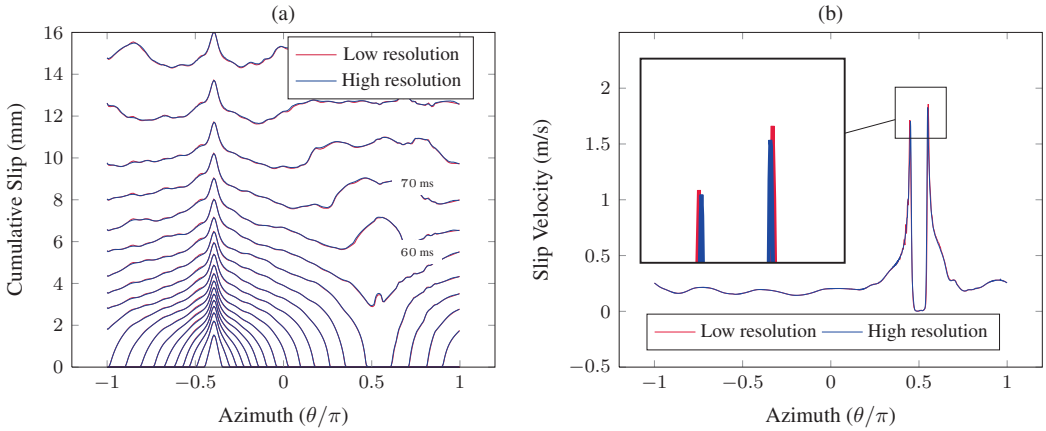


Figure 10: Cumulative slip and slip velocity as a function of the azimuthal angle θ along the plug margin. (a) The drumbeat earthquake is nucleated at $\theta=-\pi/2$, which is at the most northern position. Rupture tips meet at $\theta=\pi/2$. Each contour of cumulative slip is shown about every 5 ms. (b) Slip velocity V slightly before the entire plug margin has ruptured.

clearly illustrates the benefits of a provably stable method that can handle complex fault geometries.

To assess the accuracy of the solution we perform both high and low resolution simulations. The low resolution simulation uses $\sim 6\times 10^6$ grid points with 1.7×10^3 grid points placed on the plug margin. We use a time step of $\Delta t = 1.75\times 10^{-2}$ ms. The minimum length of an edge is $h_{\min}=2$ cm and the maximum grid spacing is $h_{\max}=30$ cm. The high resolution simulation has twice the resolution, with $\sim 25\times 10^6$ grid points and a time step of $\Delta t = 8.8\times 10^{-3}$ ms. In these simulations we study the accuracy of slip velocity V and cumulative slip $\int_0^t V(\cdot,t)dt$ at different times during the rupture process. Fig. 10(a) shows cumulative slip every ≈ 5 ms for the first 90 ms of both simulations. The position along the plug margin is parameterized using the azimuthal angle θ. Drumbeat earthquake nucleation is initiated at $\theta=-\pi/2$ (in the north) and rupture tips eventually meet at the endpoint $\theta=\pi/2$ (in the south). At 80 ms the maximum difference in average slip between the two simulations is only 0.13%.

Maximum errors occur at the rupture tip, where fields vary most rapidly and spatial gradients are largest. Fig. 10(b) shows slip velocity at time 63 ms, which is right before wave focusing occurs at the end point $\theta=\pi/2$. In the simulations the maximum difference in peak amplitude of the rupture tips is 1.7%. During the entire rupture process (0−65 ms) the maximum difference in peak amplitude is 4% on average.

6 Conclusions

We have developed a hybrid method for coupling the SBP high order finite difference method to the unstructured finite volume method for earthquake rupture dynamics and

https://doi.org/10.4208/cicp.111013.120914a Published online by Cambridge University Press

seismic wave propagation problems. The theoretical analysis and computational results were presented for antiplane problems, and can be extended to plane strain problems.

The unstructured finite volume method was used to handle complex geometry and the high order finite difference method was used everywhere else in the domain. Provably stable fault interface conditions were derived for the finite volume method by using characteristic variables and considering smooth faults. Provably stable hybrid interface conditions were derived by modifying the control volumes of the finite volume method along the hybrid interfaces. Modifying the control volumes ensures that the two corresponding SBP norms evaluated along the hybrid interface are identical.

Numerical experiments showed that the hybrid method converged with 2^{nd}-order accuracy as expected. However, the hybrid method was shown to obtain the same global accuracy as the finite volume method with much fewer nodes by coarsening the structured grids in the hybrid mesh.

Finally, we applied the developed method to model drumbeat earthquakes occurring during extrusion of a crystalline plug from a volcanic conduit. Rupture propagation along the margins of the plug involves focusing and trapping of waves within the conduit, making this a particularly challenging application problem. The problem illustrates the need for geometric flexibility in the near-field source region, where waves transfer stress along the curved plug margins to drive the propagating rupture, and high accuracy far from the fault where seismic instruments are typically located. The hybrid method provides both of these by employing an unstructured mesh immediately around the plug together with a more accurate and efficient structured mesh method outside this region.

A Fault interface treatment

The nondimensional energy dissipation rate on the fault γ is

$$\begin{aligned} FT=&\sum_{k=1}^{2}\left[\frac{1}{2}\left(\mathbf{q}_F^{(k)}\right)^T\left(\mathbf{X}_F\otimes\mathbf{A}_x+\mathbf{Y}_F\otimes\mathbf{A}_y\right)\mathbf{q}_F^{(k)}\right.\\ &\left.+\left(\mathbf{q}_F^{(k)}\right)^T\boldsymbol{\Sigma}_F^{(k)}\left(\left(\mathbf{w}_F^{-(k)}-\boldsymbol{\mathcal{W}}_F^{-(k)}\right)\otimes\mathbf{e}_3\right)\right]\\ =&\sum_{k=1}^{2}\left[\left(\mathbf{v}_z^{(k)}\right)_F^T\mathbf{X}_F^{(k)}\left(\sigma_{xz}^{(k)}\right)_F+\left(\mathbf{v}_z^{(k)}\right)_F^T\mathbf{Y}_F^{(k)}\left(\sigma_{yz}^{(k)}\right)_F\right.\\ &\left.+\left(\boldsymbol{\Sigma}_{F1}^{(k)}\left(\mathbf{v}_z^{(k)}\right)_F+\boldsymbol{\Sigma}_{F2}^{(k)}\left(\sigma_{xz}^{(k)}\right)_F+\boldsymbol{\Sigma}_{F3}^{(k)}\left(\sigma_{yz}^{(k)}\right)_F\right)^T\left(\mathbf{w}_F^{-(k)}-\boldsymbol{\mathcal{W}}_F^{(k)}\right)\right]. \end{aligned}$$

Since the fault is smooth (i.e., without kinks) the normal is uniquely defined everywhere on either side of the fault. Thus, we can define the discrete outward unit normal on the

https://doi.org/10.4208/cicp.111013.120914a Published online by Cambridge University Press

fault with respect to side (k) at a fault boundary node j as

$$n_j^{(k)}=\left[\frac{\Delta y_j^{(k)}}{\Delta s_j},-\frac{\Delta x_j^{(k)}}{\Delta s_j}\right]^T,\quad \Delta s_j=\sqrt{\left(\Delta x_j^{(k)}\right)^2+\left(\Delta y_j^{(k)}\right)^2},\quad j\in\gamma, \tag{A.1}$$

where $\Delta x_j^{(k)}$ and $\Delta y_j^{(k)}$ are given by the diagonal entries of $\mathbf{X}_F^{(k)}$ and $\mathbf{Y}_F^{(k)}$. Since the nodes on the fault are collocated, $\Delta s_j^{(1)}=\Delta s_j^{(2)}$ and $n_j^{(1)}=-n_j^{(2)}$. This follows from the definition of $\mathbf{X}_F^{(k)}$ and $\mathbf{Y}_F^{(k)}$ (see Fig. 3). We write the discrete outward unit normal on the fault boundary in terms of

$$\mathbf{N}_i^{(k)}=\left[\mathbf{S}_F^{-1}\mathbf{X}_F^{(k)},\quad \mathbf{S}_F^{-1}\mathbf{Y}_F^{(k)}\right],\quad \mathbf{S}_F=\mathbf{diag}\left[\Delta s_j\right],\quad \mathbf{x}^T\mathbf{S}_F\mathbf{x}>0\ \forall\ \mathbf{x}. \tag{A.2}$$

The matrix formulation of the unit normal in (A.2) allows us to write

$$\left(\mathbf{v}_z^{(k)}\right)_F^T\mathbf{X}_F^{(k)}\left(\sigma_{xz}^{(k)}\right)_F+\left(\mathbf{v}_z^{(k)}\right)_F^T\mathbf{Y}_F^{(k)}\left(\sigma_{yz}^{(k)}\right)_F=\left(\mathbf{v}_z^{(k)}\right)_F^T\mathbf{S}_F\mathbf{N}_i^{(k)}\left(\sigma_{iz}^{(k)}\right)_F. \tag{A.3}$$

Choosing the penalty terms $\mathbf{\Sigma}_{F1}^{(k)}=-\mathbf{S}_F/2$, $\mathbf{\Sigma}_{F2}^{(k)}=-\mathbf{X}_F^{(k)}/2$ and $\mathbf{\Sigma}_{F3}^{(k)}=-\mathbf{Y}_F^{(k)}/2$ leads to

$$\begin{aligned}FT=\sum_{k=1}^{2}\Bigg[&\left(\mathbf{v}_z^{(k)}\right)_F^T\mathbf{S}_F\mathbf{N}_i^{(k)}\left(\sigma_{iz}^{(k)}\right)_F\\&-\frac{1}{2}\left(\left(\mathbf{v}_z^{(k)}\right)_F+\mathbf{N}_F^{(k)}\left(\sigma_{iz}^{(k)}\right)_F\right)^T\mathbf{S}_F\left(\mathbf{w}_F^{-(k)}-\boldsymbol{\mathcal{W}}_F^{-(k)}\right)\Bigg].\end{aligned} \tag{A.4}$$

By changing physical variables to characteristic variables (2.4), Eq. (A.4) becomes

$$\begin{aligned}FT=-\frac{1}{4}\sum_{k=1}^{2}\Bigg[&\left(\mathbf{w}_F^{+(k)}-\boldsymbol{\mathcal{W}}_F^{-(k)}\right)^T\mathbf{S}_F\left(\mathbf{w}_F^{+(k)}+\boldsymbol{\mathcal{W}}_F^{-(k)}\right)\\&+\left(\mathbf{w}_F^{-(k)}-\boldsymbol{\mathcal{W}}_F^{-(k)}\right)^T\mathbf{S}_F\left(\mathbf{w}_F^{-(k)}-\boldsymbol{\mathcal{W}}_F^{-(k)}\right)\Bigg].\end{aligned}$$

Defining

$$\begin{aligned}&\left(\hat{\mathbf{v}}_z^{(k)}\right)_F=\frac{1}{2}\left(\boldsymbol{\mathcal{W}}_F^{-(k)}-\mathbf{w}_F^{+(k)}\right),\quad \hat{\boldsymbol{\tau}}^{(k)}=\mathbf{N}_i^{(k)}\left(\hat{\sigma}_{iz}^{(k)}\right)_F=\frac{1}{2}\left(\boldsymbol{\mathcal{W}}_F^{-(k)}+\mathbf{w}_F^{+(k)}\right),\\&\hat{\boldsymbol{V}}=\left(\hat{\mathbf{v}}_z^{(2)}\right)_F-\left(\hat{\mathbf{v}}_z^{(1)}\right)_F.\end{aligned} \tag{A.5}$$

Since $\boldsymbol{\mathcal{W}}_F^{-(k)}$ is derived to satisfy continuity (2.9) and the discrete outward unit normals satisfy $\mathbf{N}_i^{(1)}=-\mathbf{N}_i^{(2)}$, it follows that

$$\hat{\boldsymbol{\tau}}^{(1)}=-\hat{\boldsymbol{\tau}}^{(2)}=\hat{\mathbf{F}}(\hat{\mathbf{V}},\boldsymbol{\psi}). \tag{A.6}$$

https://doi.org/10.4208/cicp.111013.120914a Published online by Cambridge University Press

The vector $\mathbf{F}(\hat{\mathbf{V}},\boldsymbol{\psi})$ contains the friction coefficients evaluated at each entry of $\hat{\mathbf{V}}$. Using (A.5) and (A.6) leads to

$$FT = -\left(\hat{\mathbf{V}}\right)^T \mathbf{S}_F \mathbf{F}(\hat{\mathbf{V}},\text{-}) - \frac{1}{4}\sum_{k=1}^{2}\left(\mathbf{w}_F^{-(k)} - \boldsymbol{\mathcal{W}}_F^{-(k)}\right)^T \mathbf{S}_F \left(\mathbf{w}_F^{-(k)} - \boldsymbol{\mathcal{W}}_F^{-(k)}\right). \tag{A.7}$$

B Rate and state friction and nondimensionalization

We first present and explain the friction law using dimensional variables and parameters. We then proceed with nondimensionalizing the friction law.

The regularized slip law form of rate-and-state friction [56] is

$$f(V,\psi) = a\,\text{arcsinh}\left(\frac{V}{2V_0}\exp\left(\frac{\psi}{a}\right)\right), \tag{B.1}$$

$$\frac{d\psi}{dt} = G(V,\psi) = -\frac{V}{L}\left(f(V,\psi) - f_{ss}(V)\right), \tag{B.2}$$

where the parameter V_0 is a reference slip velocity and the constitutive parameter $a>0$ quantifies the so-called direct effect. To understand the response of a sliding interface governed by rate-and-state friction, assume that the interface is sliding steadily at a velocity V and state variable ψ that satisfies $G(V,\psi)=0$. As illustrated in Fig. 11, if V is suddenly increased from V to $V+\Delta V$, then f abruptly increases with ψ remaining the same. As sliding continues, the state variable ψ gradually evolves, over time scale $L/(V+\Delta V)$, toward a new steady state $f_{ss}(V+\Delta V)$. As described earlier, the conditions $\partial f/\partial V>0$ (which is guaranteed by $a>0$) and $Vf(V,\psi)\geq 0$ for all V are required for both the continuous and discrete energy estimates. The steady state friction coefficient is commonly

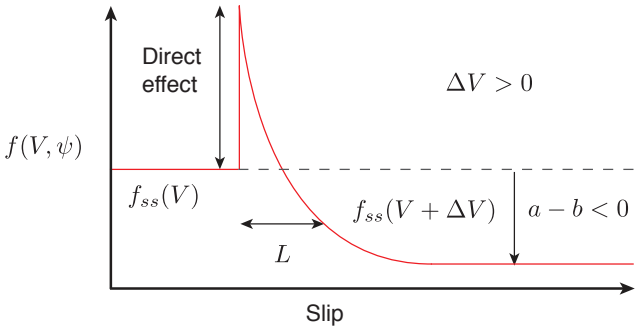


Figure 11: Demonstration of rate-and-state friction with velocity-weakening friction. Initially steady sliding at slip velocity V is followed by an instantaneous increase in slip velocity by $\Delta V>0$, causing the friction coefficient to increase instantaneously (the direct effect). After slip of order L (the state evolution distance), the friction coefficient relaxes toward a new steady state $f_{ss}(V+\Delta V)$, where $f_{ss}(V+\Delta V)<f_{ss}(V)$.

https://doi.org/10.4208/cicp.111013.120914a Published online by Cambridge University Press

taken to be

$$f_{ss}(V)=f_0-(b-a)\ln\left(\frac{V}{V_0}\right), \tag{B.3}$$

where f_0 is the reference friction coefficient. If $b-a>0$ then the steady state friction coefficient decreases with increasing velocity and the frictional response is called velocity weakening. That is a necessary condition for unstable sliding and earthquake occurrence.

Linear stability analysis has been used to study conditions for unstable sliding along planar faults with rate-and-state friction [56, 58]. For steady state velocity-weakening faults, slow steady sliding is unstable to Fourier mode perturbations having wavelengths greater than

$$h^*\approx\frac{GL}{(b-a)\sigma_0}. \tag{B.4}$$

This length scale must be resolved by at least several grid points in numerical simulations; otherwise short-wavelength numerical oscillations will grow in an unstable manner. Since the length scale h^* emerges from analysis of the linearized equations, while actual rupture problems involve extreme nonlinearity, it is necessary in practice to use a grid spacing $h\ll h^*$. In (B.4), σ_0 is the normal stress (positive in compression) and $(b-a)\sigma_0$ is the characteristic stress change, which provides the stress scale for nondimensionalization. Characteristic particle and slip velocities are thus $(b-a)\sigma_0/\rho c$.

We next nondimensionalize (B.2). Since V_0 is an arbitrary reference velocity (which then determines the associated reference friction coefficient f_0 from laboratory data), we use $V_0=(b-a)\sigma_0/\rho c$. After nondimensionalizing in this manner, the dimensionless friction law is

$$\begin{aligned} &f(V,\psi)=a\,\mathrm{arcsinh}\left(\frac{V}{2}\exp\left(\frac{\psi}{a}\right)\right), \quad \frac{d\psi}{dt}=-V\left(f(V,\psi)-f_{ss}(V)\right),\\ &f_{ss}(V)=f_0-(b-a)\ln(V). \end{aligned} \tag{B.5}$$

Here, V is now the non-dimensional slip velocity.

C Method of manufactured solutions

Throughout this section all variables and parameters are dimensionless. In order to construct our manufactured solution, we consider steady sliding of a plug of constant radius R through the surrounding material (Fig. 2) and then we add perturbations satisfying the wave equation exactly without adding any source terms. The solution we will develop is continuous and infinitely differentiable everywhere except at the margins of the plug (fault). Additionally, the solution will be constructed such that the tractions exerted on the walls of the plug and surrounding material satisfy force balance (2.9).

https://doi.org/10.4208/cicp.111013.120914a Published online by Cambridge University Press

We solve this problem using polar coordinates and rewriting the first-order hyperbolic problem as the scalar wave equation: $\partial^2 u_z^{(k)}/\partial t^2 = \nabla^2 u_z^{(k)}$, where the full-space and plug solutions $u_z^{(k)}$ are the displacement fields in the $\hat{z}$ direction. In addition, $\nabla^2 = \partial^2/\partial_x^2 + \partial^2/\partial_y^2$). We look for axisymmetric solutions $u_z^{(k)}(r,t)$ to the wave equation without source terms that depend only the radial distance $r=\sqrt{x^2+y^2}$ from the center of the plug and with purely oscillatory time-dependence $\exp(i\omega t)$, where ω is the angular frequency of oscillations. The solution is

$$u_z^{(1)}(r,t) = \Delta u_z^{(1)}(r,t) + \tau_{bg} r + \frac{1}{2} V_{bg} t, \quad \text{if } r \geq R, \tag{C.1}$$

$$u_z^{(2)}(r,t) = \Delta u_z^{(2}(r,t) + \tau_{bg} r - \frac{1}{2} V_{bg} t, \quad \text{if } r \leq R, \tag{C.2}$$

$$\Delta u_z^{(1)}(r,t) = \frac{\Delta V_0 J_1(\omega R)\left(Y_0(\omega r)\sin(\omega t) + J_0(\omega r)\cos(\omega t)\right)}{\omega\left(J_1(\omega R)Y_0(\omega R) - J_0(\omega R)Y_1(\omega R)\right)},$$

$$\Delta u_z^{(2)}(r,t) = \frac{\Delta V_0 J_0(\omega r)\left(Y_1(\omega R)\sin(\omega t) + J_1(\omega R)\cos(\omega t)\right)}{\omega\left(J_1(\omega R)Y_0(\omega R) - J_0(\omega R)Y_1(\omega R)\right)}.$$

This solution describes steady sliding perturbed by axisymmetric, cylindrical standing waves. The functions J_ν and Y_ν (for $\nu = 0,\ 1$) are Bessel functions of the first and second kind, respectively. The role of the constants ΔV_0, τ_{bg} and V_{bg} is explained below.

Solutions (C.1) and (C.1) do not satisfy the friction law, so it is necessary to add source terms to the state evolution law (B.5):

$$\frac{d\psi}{dt} = -V\left(f(V,\psi) - f_{ss}(V)\right) + s, \tag{C.3}$$

$$s = V^*\left(f(V^*,\psi^*) - f_{ss}(V^*)\right) + \frac{d\psi^*}{dt}, \quad \psi^* = a\,\ln\left(\frac{2}{V^*}\sinh\left(\frac{(b-a)\tau^*}{a}\right)\right). \tag{C.4}$$

All fields in s marked with a superscript $*$ are computed from known solutions (C.1) and (C.2) using

$$v_z^{*(k)} = \frac{\partial \Delta u_z^{(k)}}{\partial t}, \quad \sigma_{xz}^{*(k)} = \frac{\partial \Delta u_z^{(k)}}{\partial x}, \quad \sigma_{yz}^{*(k)} = \frac{\partial \Delta u_z}{\partial y}, \quad \tau^* = \Delta\tau^* + \tau_{bg}, \quad V^* = \Delta V^* + V_{bg}, \tag{C.5}$$

$$\Delta\tau^* = \left.\frac{\partial \Delta u_z}{\partial r}\right|_{r=R}, \quad \Delta V^* = \left.\frac{\partial \Delta u_z^{(2)}}{\partial t}\right|_{r=R} - \left.\frac{\partial \Delta u_z^{(1)}}{\partial t}\right|_{r=R} = \Delta V_0 \cos(wt). \tag{C.6}$$

By choosing background fields τ_{bg} and V_{bg} to be

$$\tau_{bg} = \max_{t\in T}|\Delta\tau^*| + \epsilon_1, \quad V_{bg} = \Delta V_0 + \epsilon_2, \quad \epsilon_l > 0, \quad T = \left[0,\ \frac{2\pi}{\omega}\right], \tag{C.7}$$

Eq. (2.17) is satisfied by the manufactured solution since $\tau^* V^* \geq 0$ for all times. At the outer boundaries the time-dependent characteristic boundary condition is used:

$$w^- = \sigma_{iz}^* n_i + v_z^*. \tag{C.8}$$

https://doi.org/10.4208/cicp.111013.120914a Published online by Cambridge University Press

In all experiments involving the manufactured solution we use $\Delta V_0 = 42$, $\epsilon_1 = 46$, $\epsilon_2 = 8\times10^{-3}$, and $\omega = 1.25\pi$. This makes V^* range from 8×10^{-3} to $42+8\times10^{-3}$. Values for frictional parameters are listed in Table 5.

References

[1] B.T. Aagaard, Finite-element simulations of earthquakes, Ph.D. thesis, 1999.
[2] D. Amsallem, J. Nordström, High-order accurate difference schemes for the hodgkin–huxley equations, J. Comput. Phys. 252 (2013) 573–590.
[3] D. Andrews, Rupture propagation with finite stress in antiplane strain, J. Geophys. Res. 81 (1976) 3575–3582.
[4] H. Aochi, E. Fukuyama, Three-dimensional nonplanar simulation of the 1992 Landers earthquake, J. Geophys. Res. 107 (2002) 2001.
[5] D. Appelö, T. Hagstrom, G. Kreiss, Perfectly matched layers for hyperbolic systems: general formulation, well-posedness, and stability, SIAM J. Appl. Math. (2006) 1–23.
[6] L. Badea, I.R. Ionescu, S. Wolf, Schwarz method for earthquake source dynamics, J. Comput. Phys. 227 (2008) 3824–3848.
[7] M. Barall, A grid-doubling finite-element technique for calculating dynamic three-dimensional spontaneous rupture on an earthquake fault, Geophysical Journal International 178 (2009) 845–859.
[8] M. Benjemaa, N. Glinsky-Olivier, V. Cruz-Atienza, J. Virieux, 3-D dynamic rupture simulations by a finite volume method, Geophys. J. Int. 178 (2009) 541–560.
[9] M. Benjemaa, N. Glinsky-Olivier, V. Cruz-Atienza, J. Virieux, S. Piperno, Dynamic non-planar crack rupture by a finite volume method, Geophys. J. Int. 171 (2007) 271–285.
[10] M. Carpenter, D. Gottlieb, S. Abarbanel, Time-stable boundary conditions for finite-difference schemes solving hyperbolic systems: methodology and application to high-order compact schemes, J. Comput. Phys. (1993).
[11] M. Carpenter, C. Kennedy, Fourth-order 2N-storage Runge-Kutta schemes, Nasa Technical Memorandum 109112 (1994).
[12] M. Carpenter, J. Nordström, D. Gottlieb, A stable and conservative interface treatment of arbitrary spatial accuracy, J. Comput. Phys. 148 (1999) 341–365.
[13] M.H. Carpenter, J. Nordström, D. Gottlieb, Revisiting and extending interface penalties for multi-domain summation-by-parts operators, J. Sci. Comput. 45 (2010) 118–150.
[14] V. Cruz-Atienza, J. Virieux, Dynamic rupture simulation of non-planar faults with a finite-difference approach, Geophys. J. Int. 158 (2004) 939–954.
[15] V. Cruz-Atienza, J. Virieux, H. Aochi, 3D finite-difference dynamic-rupture modeling along nonplanar faults, Geophys. 72 (2007) SM123–SM137.
[16] S. Day, Three-dimensional finite difference simulation of fault dynamics: rectangular faults with fixed rupture velocity, Bull. Seismol. Soc. Am. 72 (1982) 705–727.
[17] J. De La Puente, J. Ampuero, M. Käser, Dynamic rupture modeling on unstructured meshes using a discontinuous Galerkin method, J. geophys. Res 114 (2009) B10302.
[18] B. Duan, D. Oglesby, Nonuniform prestress from prior earthquakes and the effect on dynamics of branched fault systems, J. Geophys. Res 112 (2007) B05308.
[19] G.P. Ely, S.M. Day, J.B. Minster, A support-operator method for viscoelastic wave modelling in 3-D heterogeneous media, Geophys. J. Int. 172 (2008) 331–344.

https://doi.org/10.4208/cicp.111013.120914a Published online by Cambridge University Press

[20] G. Festa, J.P. Vilotte, The Newmark scheme as velocity–stress time-staggering: an efficient PML implementation for spectral element simulations of elastodynamics, Geophys. J. Int. 161 (2005) 789–812.
[21] G.J. Gassner, A skew-symmetric discontinuous galerkin spectral element discretization and its relation to sbp-sat finite difference methods, SIAM Journal on Scientific Computing 35 (2013) A1233–A1253.
[22] P.H. Geubelle, J.R. Rice, A spectral method for three-dimensional elastodynamic fracture problems, Journal of the Mechanics and Physics of Solids 43 (1995) 1791–1824.
[23] J. Gong, J. Nordström, A stable and efficient hybrid scheme for viscous problems in complex geometries, J. Comput. Phys. 226 (2007) 1291–1309.
[24] J. Gong, J. Nordström, Interface procedures for finite difference approximations of the advection–diffusion equation, J. Comput. Appl. Math. 236 (2011) 602–620.
[25] B. Gustafsson, The convergence rate for difference approximations to mixed initial boundary value problems, Math. Comp 29 (1975) 396–406.
[26] B. Gustafsson, H. Kreiss, J. Oliger, Time dependent problems and difference methods, volume 24, Wiley-Interscience, 1995.
[27] T. Hagstrom, A. Mar-Or, D. Givoli, High-order local absorbing conditions for the wave equation: Extensions and improvements, J. Comput. Phys. 227 (2008) 3322–3357.
[28] R. Harris, M. Barall, R. Archuleta, E. Dunham, B. Aagaard, J. Ampuero, H. Bhat, V. Cruz-Atienza, L. Dalguer, P. Dawson, et al., The SCEC/USGS dynamic earthquake rupture code verification exercise, Seismol. Res. Lett. 80 (2009) 119–126.
[29] J.S. Hesthaven, T. Warburton, Nodal discontinuous Galerkin methods: algorithms, analysis, and applications, volume 54, Springer, 2007.
[30] H. Igel, M. Käser, M. Stupazzini, Seismic wave propagation in media with complex geometries, simulation of., 2009.
[31] R. Iverson, D. Dzurisin, C. Gardner, T. Gerlach, R. LaHusen, M. Lisowski, J. Major, S. Malone, J. Messerich, S. Moran, et al., Dynamics of seismogenic volcanic extrusion at Mount St Helens in 2004–05, Nat. 444 (2006) 439–443.
[32] N. Kame, T. Yamashita, Simulation of the spontaneous growth of a dynamic crack without constraints on the crack tip path, Geophys. J. Int. 139 (1999) 345–358.
[33] Y. Kaneko, N. Lapusta, J.P. Ampuero, Spectral element modeling of spontaneous earthquake rupture on rate and state faults: Effect of velocity-strengthening friction at shallow depths, J. Geophys. Res. 113 (2008) B09317.
[34] M. Käser, P. Mai, M. Dumbser, Accurate calculation of fault-rupture models using the high-order discontinuous Galerkin method on tetrahedral meshes, Bull. Seismol. Soc. Am. 97 (2007) 1570–1586.
[35] J.E. Kozdon, E.M. Dunham, J. Nordström, Interaction of waves with frictional interfaces using summation-by-parts difference operators: Weak enforcement of nonlinear boundary conditions, J. Sci. Comput. 50 (2012) 341–367.
[36] J.E. Kozdon, E.M. Dunham, J. Nordström, Simulation of dynamic earthquake ruptures in complex geometries using high-order finite difference methods, J. Sci. Comput. 55 (2013) 92–124.
[37] H. Kreiss, Initial boundary value problems for hyperbolic systems, Commun. Pure Appl. Math. 23 (1970) 277–298.
[38] H. Kreiss, G. Scherer, Finite element and finite difference methods for hyperbolic partial differential equations, Academic Press, 1974.
[39] H. Kreiss, G. Scherer, On the existence of energy estimates for difference approximations for

https://doi.org/10.4208/cicp.111013.120914a Published online by Cambridge University Press

hyperbolic systems, Tech. Rep. (1977).
[40] S. Ma, R. Archuleta, Finite element modeling of earthquake dynamic rupture on 2D nonplanar dipping faults, in: AGU Fall Meeting Abstracts, volume 1, p. 0938.
[41] S. Ma, R.J. Archuleta, P. Liu, Hybrid modeling of elastic p-sv wave motion: a combined finite-element and staggered-grid finite-difference approach, Bull. Seismol. Soc. Am. 94 (2004) 1557–1563.
[42] R. Madariaga, K. Olsen, R. Archuleta, Modeling dynamic rupture in a 3D earthquake fault model, Bull. Seismol. Soc. Am. 88 (1998) 1182–1197.
[43] K. Mattsson, J. Nordström, High order finite difference methods for wave propagation in discontinuous media, J. Comput. Phys. 220 (2006) 249–269.
[44] P. Moczo, J. Kristek, M. Galis, P. Pazak, M. Balazovjech, The finite-difference and finite-element modeling of seismic wave propagation and earthquake motion, Acta Phys. Slovaca 57 (2007).
[45] S. Moran, S. Malone, A. Qamar, W. Thelen, A. Wright, J. Caplan-Auerbach, Seismicity associated with renewed dome building at Mount St. Helens, 2004-2005, Prof. Pap. U.S Geol. Surv. (2008) 27–60.
[46] J. Nordström, Error bounded schemes for time-dependent hyperbolic problems, SIAM J. Sci. Comput. 30 (2007) 46–59.
[47] J. Nordström, Linear and nonlinear boundary conditions for wave propagation problems, in: Recent Developments in the Numerics of Nonlinear Hyperbolic Conservation Laws, Springer, 2013, pp. 283–299.
[48] J. Nordström, K. Forsberg, C. Adamsson, P. Eliasson, Finite volume methods, unstructured meshes and strict stability for hyperbolic problems, Appl. Numer. Math. 45 (2003) 453–473.
[49] J. Nordström, J. Gong, A stable hybrid method for hyperbolic problems, J. Comput. Phys. 212 (2006) 436–453.
[50] J. Nordström, J. Gong, E. Van der Weide, M. Svärd, A stable and conservative high order multi-block method for the compressible Navier–Stokes equations, J. Comput. Phys. 228 (2009a) 9020–9035.
[51] J. Nordström, R. Gustafsson, High order finite difference approximations of electromagnetic wave propagation close to material discontinuities, J. Sci. Comput. 18 (2003) 215–234.
[52] J. Nordström, F. Ham, M. Shoeybi, E. Van der Weide, M. Svärd, K. Mattsson, G. Iaccarino, J. Gong, A hybrid method for unsteady inviscid fluid flow, Comput. Fluids 38 (2009b) 875–882.
[53] J. Nordström, K. Mattsson, C. Swanson, Boundary conditions for a divergence free velocity–pressure formulation of the Navier–Stokes equations, J. Comput. Phys. 225 (2007) 874–890.
[54] P. Olsson, Summation by parts, projections, and stability. I, Math. Comput. 64 (1995) 1035–1035.
[55] C. Pelties, J. de la Puente, J.P. Ampuero, G.B. Brietzke, M. Kser, Three-dimensional dynamic rupture simulation with a high-order discontinuous Galerkin method on unstructured tetrahedral meshes, J. Geophys. Res. 117 (2012) B02309.
[56] J. Rice, N. Lapusta, K. Ranjith, Rate and state dependent friction and the stability of sliding between elastically deformable solids, J. Mech. Phys. Solids 49 (2001) 1865–1898.
[57] P.J. Roache, Verification and validation in computational science and engineering, Hermosa Publishers, 1998.
[58] A. Ruina, Stability of steady frictional slipping, J. Appl. Mech. 50 (1983) 343–349.
[59] B. Strand, Summation by parts for finite difference approximations for d/dx, J. Comput. Phys. 110 (1994) 47–67.

https://doi.org/10.4208/cicp.111013.120914a Published online by Cambridge University Press

[60] M. Svärd, M.H. Carpenter, J. Nordström, A stable high-order finite difference scheme for the compressible Navier–Stokes equations, far-field boundary conditions, J. Comput. Phys. 225 (2007) 1020–1038.
[61] M. Svärd, J. Nordström, On the order of accuracy for difference approximations of initial boundary value problems, J. Comput. Phys. 218 (2006) 333–352.
[62] M. Svärd, J. Nordström, A stable high-order finite difference scheme for the compressible Navier–Stokes equations: No-slip wall boundary conditions, J. Comput. Phys. 227 (2008) 4805–4824.
[63] M. Svärd, J. Nordström, Review of summation-by-parts schemes for initialboundary-value problems, J. Comput. Phys. 268 (2014) 17 – 38.
[64] T. Tada, E. Fukuyama, R. Madariaga, Non-hypersingular boundary integral equations for 3-D non-planar crack dynamics, Comput. Mech. 25 (2000) 613–626.
[65] J. Tago, V. Cruz-Atienza, J. Virieux, V. Etienne, F. Sánchez-Sesma, A 3D hp-adaptive discontinuous Galerkin method for modeling earthquake dynamics, J. Geophys. Res. 117 (2012) B09312.
[66] E. Templeton, A. Baudet, H. Bhat, R. Dmowska, J. Rice, A. Rosakis, C. Rousseau, Finite element simulations of dynamic shear rupture experiments and dynamic path selection along kinked and branched faults, J. Geophys. Res. 114 (2009) B08304.
[67] E. Templeton, H. Bhat, R. Dmowska, J. Rice, Dynamic rupture through a branched fault configuration at Yucca Mountain, and resulting ground motions, Bull. Seismol. Soc. Am. 100 (2010) 1485–1497.
[68] J.F. Thompson, B.K. Soni, N.P. Weatherill, Handbook of Grid Generations, CRC press, 1999.
[69] J. Virieux, R. Madariaga, Dynamic faulting studied by a finite difference method, Bull. Seismol. Soc. Am. 72 (1982) 345–369.
[70] H. Zhang, X. Chen, Dynamic rupture on a planar fault in three-dimensional half spacei. theory, Geophys. J. Internat. 164 (2006) 633–652.

https://doi.org/10.4208/cicp.111013.120914a Published online by Cambridge University Press